Total variation-based reconstruction and phase retrieval for diffraction tomography

Robert Beinert* Michael Quellmalz*

beinert@math.tu-berlin.de quellmalz@math.tu-berlin.de

In optical diffraction tomography (ODT), the three-dimensional scattering potential of a microscopic object rotating around its center is recovered by a series of illuminations with coherent light. Reconstruction algorithms such as the filtered backpropagation require knowledge of the complex-valued wave at the measurement plane, whereas often only intensities, i.e., phaseless measurements, are available in practice.

We propose a new reconstruction approach for ODT with unknown phase information based on three key ingredients. First, the light propagation is modeled using Born's approximation enabling us to use the Fourier diffraction theorem. Second, we stabilize the inversion of the non-uniform discrete Fourier transform via total variation regularization utilizing a primal-dual iteration, which also yields a novel numerical inversion formula for ODT with known phase. The third ingredient is a hybrid input-output scheme. We achieved convincing numerical results, which indicate that ODT with phaseless data is possible. The so-obtained 2D and 3D reconstructions are even comparable to the ones with known phase.

Math Subject Classifications. 42B05, 47J06, 65T50, 92C55
Keywords. Phase retrieval, diffraction tomography, total variation, nonequispaced discrete Fourier transform, optical imaging

1 Introduction

Illuminating three-dimensional (3D) objects from different angles, we are interested in tomographic reconstructions. In classical X-ray computerized tomography, the light is

*TU Berlin, Institute of Mathematics, MA 4-3, Straße des 17. Juni 136, D-10623 Berlin, Germany.

assumed to propagate along straight lines enabling reconstruction via the inverse Radon transform. This assumption relies on the fact that the employed X-rays have a very short wavelength, which is much smaller than any object features of interest. In *optical diffraction tomography* (ODT), the image is obtained via visible light of wavelengths of hundreds of nanometers being the size of studied features such as subcellular structures. Therefore, we rely on a more sophisticated light propagation model taking the occurring diffraction into account.

Mathematically speaking, we aim to recover the three-dimensional scattering potential of the unknown object given two-dimensional measurements of the complex wave function at a plane behind the object for different illumination directions. We assume that the illumination directions are known beforehand, motion detection methods were discussed in [22]. To model the light propagation, we take advantage of the Born approximation, which is valid for objects of small size and variation of the scattering potential. A well-established inversion method for the Born-based ODT model is the backpropagation [19], which is still widely used in practice [24, 59]. The backpropagation, however, relies on complex-valued measurements whereas only phaseless intensities are available in most practical setups. This means that the object reconstruction becomes more ill posed and is coupled with a phase retrieval problem.

Phase retrievals of different kinds have been intensely studied in the literature. In general, solutions are highly ambiguous. Characterizations of the whole solution set and uniqueness guarantees under additional constraints like known support or non-negativity have been studied for functions with continuous domains [1, 36, 49, 50, 65], where the measurements correspond to the intensity of the Fourier transform. Analogous results exist for fractional Fourier intensities [44] for instance. Even if the Fourier phase retrieval problem is discretized, the ambiguousness remains an issue independently of how many measurements are available [3, 6–8, 21, 36]. To overcome these problems, more general phase retrieval problems, where the intensity of arbitrary linear measurements are given, have been studied. Under certain assumptions on the linear measurements, the phase retrieval problem becomes unique [13, 14, 25, 26]. Using a tensorial lifting, the problem may be exemplarily solved using semi-definite programming [13, 14], tensor-free primal-dual methods [5], or polarization techniques [2, 61]. Moreover, the phase retrieval problem is well understood in the context of frames [2, 36, 61].

Unfortunately, phase retrieval in ODT does not fit in the above setups since the given measurements with respect to the Born approximation are non-linear. Therefore, the well-established theoretical results regarding ambiguousness, uniqueness, and stability cannot be transferred to our problem. In X-ray tomography, where the intensity measurements are modeled using the Radon transform of the unknown object followed by diffraction, uniqueness of the reconstruction is guaranteed [58]. The difference in the employed mathematical model, however, prevents a direct application of the uniqueness results in ODT.

For retrieving an unknown phase in ODT, different approaches have been studied. An iterative method of propagation and backpropagation in free space between the mea-

surements plane and a parallel plane through the object was proposed by Maleki and Devaney [57]. The Gabor holography compared unfavorably in numerical tests [67]. A phase retrieval method utilizing ideas of Fourier ptychography was developed in [42]. Other approaches rely on the acquisition of more data using two parallel measurement planes [32] or the phase shifting interferometry (PSI) requiring 4 intensity images per illumination direction. Furthermore, phase retrieval based on a far zone approximation of Born [16] or using the X-ray transform [37] has been studied.

In this paper, we consider the phase retrieval problem in ODT, where the absolute value of the wave is measured at one plane per illumination direction, and we assume that the Born approximation is valid. Our proposed method is based on the hybrid input-output algorithm from Fourier phase retrieval combined with a total variation (TV) regularization utilizing a primal-dual method. TV regularization has already been applied to limited angle reconstruction in ODT utilizing an approximate Radon transform [53].

The main contributions of this paper are as follows:

- We consider the inverse nonuniform discrete Fourier transform (NDFT) as an inverse problem and apply TV-based regularization methods to improve the inversion especially in the presence of noise. We apply this regularized NDFT inversion to obtain a novel reconstruction method for ODT with known phase.
- We propose a numerical algorithm for solving the phase retrieval problem in ODT. This algorithm makes use of an adaption of the hybrid input-output scheme and the TV-regularized inversion of the NDFT.
- Our numerical simulations indicate that phase retrieval is possible and greatly benefits from the regularized ODT inversion. In total, the reconstruction quality is comparable to the known-phase inversion.

Outline of the paper. The employed notation is introduced in Section 2. The basics on diffraction tomography and the theoretical foundation of the inversion methods are explained in Section 3. We introduce the discretized setting used for implementations in Section 4. Since the inversion of the NDFT is the key element for reconstruction in diffraction tomography, we discuss different computation methods for the inverse NDFT in Section 5. On the basis of these methods, different numerical ODT inversions for complex-valued data are studied and compared. The proposed phase retrieval method for ODT is derived in Section 6. Finally, numerical simulations in Section 7 show that phase retrieval in ODT is possible and we achieve favorable reconstruction results. Conclusions are given in Section 8.

2 Notation and preliminary remarks

In the following, we use the (symmetric) index set

$$\mathcal{I}_K := \{-K/2, -K/2+1, \dots, K/2-1\},$$

where $K \in 2\mathbb{N}$. Although $\mathcal{I}_K$ may be adapted for odd K, we only consider the even case for convenience. The set of the first $M \in \mathbb{N}$ positive integers is further denoted by

$$\mathcal{J}_M \coloneqq \{1, 2, \dots, M\}.$$

Numerically, we represent the unknown object as *d-dimensional signal*

$$\boldsymbol{x} \coloneqq [x_{\boldsymbol{k}}]_{\boldsymbol{k} \in \mathcal{I}_K^d} \in \mathbb{R}^{K^d},$$

which may be interpreted as samples of a multivariate function. The *(weighted) 2-norm* of the d-dimensional signal $\boldsymbol{x}$ is defined by

$$\|\boldsymbol{x}\|_2^2 \coloneqq \sum_{\boldsymbol{k} \in \mathcal{I}_K^d} |x_{\boldsymbol{k}}|^2 \qquad \text{and} \qquad \|\boldsymbol{x}\|_{2,\boldsymbol{w}}^2 \coloneqq \sum_{\boldsymbol{k} \in \mathcal{I}_K^d} w_{\boldsymbol{k}} |x_{\boldsymbol{k}}|^2$$

for some non-negative weights $\boldsymbol{w} \in \mathbb{R}_{\geqslant 0}^{K^d}$.

Besides the signals, we also require the notion of a d-dimensional *discrete vector field* $\boldsymbol{y} \in \mathbb{R}^{K^d \times d}$, where the elements of $\boldsymbol{y}$ are itself d-dimensional vectors, i.e. $y_{\boldsymbol{k}} \in \mathbb{R}^d$ for $\boldsymbol{k} \in \mathcal{I}_K^d$. The signal $\boldsymbol{y}_{\cdot,\ell}$ consisting of the ℓth components is defined by $[\boldsymbol{y}_{\cdot,\ell}]_{\boldsymbol{k}} \coloneqq [y_{\boldsymbol{k}}]_\ell$ for $\boldsymbol{k} \in \mathcal{I}_K^d$ and $\ell \in \mathcal{J}_d$. The *(1,2)- and (2,2)-norm* of a discrete vector field is given by

$$\|\boldsymbol{y}\|_{1,2} \coloneqq \sum_{\boldsymbol{k} \in \mathcal{I}_K^d} \|y_{\boldsymbol{k}}\|_2 \qquad \text{and} \qquad \|\boldsymbol{y}\|_{2,2}^2 \coloneqq \sum_{\boldsymbol{k} \in \mathcal{I}_K^d} \|y_{\boldsymbol{k}}\|_2^2.$$

We use analogous definitions for signals whose domains are not $\mathcal{I}_K^d$.

Finally, we interpret all occurring complex vector spaces $\mathbb{C}^N$ as $2N$-dimensional vector spaces over $\mathbb{R}$ with the inner product

$$\langle \boldsymbol{x}, \boldsymbol{y} \rangle \coloneqq \sum_{n=1}^{N} \operatorname{Re}[x_n \bar{y}_n]$$

for $\boldsymbol{x}, \boldsymbol{y} \in \mathbb{C}^N$, which is necessary to apply certain techniques and numerical methods from convex analysis. For $\boldsymbol{A} \in \mathbb{C}^{N \times K}$ declaring the mapping $\boldsymbol{x} \mapsto \boldsymbol{A}\boldsymbol{x}$ from $\mathbb{R}^K$ to $\mathbb{C}^N$, the adjoint mapping becomes $\boldsymbol{y} \mapsto \operatorname{Re}[\boldsymbol{A}^* \boldsymbol{y}]$ from $\mathbb{C}^N$ to $\mathbb{R}^K$.

3 Diffraction tomography

In this section, we describe the setup in *optical diffraction tomography* (ODT), cf. [48]. We want to reconstruct an object's *scattering potential* $f \colon \mathbb{R}^d \to \mathbb{R}$, where we restrict our considerations to the practically meaningful dimensions $d \in \{2, 3\}$. The object is embedded in a homogeneous background and is illuminated by a monochromatic plane wave. The *incident field*

$$u^{\mathrm{inc}}(\boldsymbol{x}) = \mathrm{e}^{\mathrm{i} k_0 x_d}, \qquad \boldsymbol{x} \in \mathbb{R}^d, \tag{1}$$

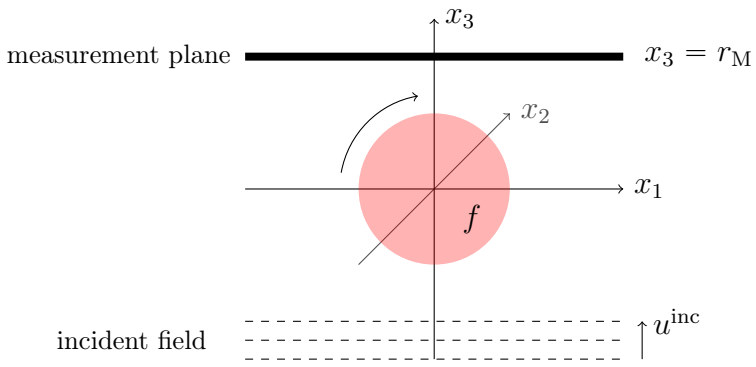

Figure 1: Experimental setup for $d = 3$ with measurement plane located at $x_3 = r_{\mathrm{M}}$.

with *wave number* $k_0 > 0$ propagates in the direction of x_d. The scattering potential admits the relation $f(\boldsymbol{x}) = k_0^2\,(n(\boldsymbol{x})/n_0 - 1)$, where $n(\boldsymbol{x})$ is the space-dependent refractive index and n_0 is the constant refractive index of the surrounding medium. In most practical cases, such as the imaging of biological cells in water, the refractive index in the object is greater than in its surrounding, cf. [56], so we will assume that $f \geqslant 0$.

For the tomographic reconstruction, we rotate the unknown object during the measurement process. The rotation at time $t \in [0, T]$ for $T > 0$ is described by the known rotation matrix $R_t \in \mathrm{SO}(d)$. The rotated object has the scattering potential $f(R_t \cdot)$. The resulting total field at time t is denoted by $u_t^{\mathrm{tot}} \colon \mathbb{R}^d \to \mathbb{C}$. We decompose the total field into

$$u_t^{\mathrm{tot}} = u^{\mathrm{inc}} + u_t^{\mathrm{sca}}$$

with the known incident field u^{inc} given in (1) and the scattered field u_t^{sca}.

The total field u_t^{tot} at time t is measured at a fixed plane behind the object. More precisely, we detect either $u_t^{\mathrm{tot}}(\boldsymbol{x}', r_{\mathrm{M}})$ or $|u_t^{\mathrm{tot}}(\boldsymbol{x}', r_{\mathrm{M}})|$ for all $\boldsymbol{x}' \in \mathbb{R}^{d-1}$ and a fixed $r_{\mathrm{M}} > 0$; the measurement plane is thus orthogonal to the x_d axis. Since the plane lies outside the object, f is assumed to be bounded and compactly supported in the ball $\mathcal{B}_{r_{\mathrm{M}}}^d = \{\boldsymbol{x} \in \mathbb{R}^d : \|\boldsymbol{x}\|_2 < r_{\mathrm{M}}\}$. The experimental setup is illustrated in Figure 1.

3.1 Born approximation

To model the scattered wave u_t^{sca}, we employ the first order *Born approximation* [45], where u_t^{sca} solves the *Helmholtz equation*

$$(\Delta + k_0^2)\, u_t^{\mathrm{sca}} = -f u^{\mathrm{inc}}. \tag{2}$$

Under the Sommerfeld radiation condition, which basically says that the scattered field is an outgoing wave, the Helmholtz equation (2) has a unique solution, see [18, Chap.

2]. This solution may be computed by using the outgoing *Green function* G_d of the Helmholtz equation, see [60, Sect. 3.3], which is given by

$$G_3(\boldsymbol{x}) := \frac{\mathrm{e}^{\mathrm{i}k_0\|\boldsymbol{x}\|_2}}{4\pi\,\|\boldsymbol{x}\|_2}, \qquad \boldsymbol{x} \in \mathbb{R}^3\backslash\{\boldsymbol{0}\},$$

and

$$G_2(\boldsymbol{x}) := \frac{\mathrm{i}}{4} H_0^{(1)}(k_0\,\|\boldsymbol{x}\|_2), \qquad \boldsymbol{x} \in \mathbb{R}^2\backslash\{\boldsymbol{0}\},$$

where $H_0^{(1)}(x) := (\pi\mathrm{i})^{-1}\int_{-\infty}^{\infty} \mathrm{e}^{\mathrm{i}x\cosh t}\,\mathrm{d}t$, $x > 0$, denotes the zeroth order Hankel function of the first kind [35, (8.421.1)]. The scattered field u_t^{sca} is then given by the convolution

$$u_t^{\mathrm{sca}}(\boldsymbol{x}) = \left[(f(R_t\cdot)\,u^{\mathrm{inc}}) * G_d\right](\boldsymbol{x}) := \int_{\mathbb{R}^d} f(R_t\boldsymbol{y})\,u^{\mathrm{inc}}(\boldsymbol{y})\,G_d(\boldsymbol{x}-\boldsymbol{y})\,\mathrm{d}\boldsymbol{y}, \qquad \boldsymbol{x} \in \mathbb{R}^d. \quad (3)$$

Restricting the convolution to the measurement plane, we model the given ODT data using the (non-linear) forward map $\mathcal{D}^{\mathrm{tot}}$ defined by

$$\mathcal{D}^{\mathrm{tot}} f(\boldsymbol{x}', t) := [(f(R_t\cdot)\,u^{\mathrm{inc}}) * G_d](\boldsymbol{x}', r_{\mathrm{M}}) + u^{\mathrm{inc}}(\boldsymbol{x}', r_{\mathrm{M}}), \qquad \boldsymbol{x}' \in \mathbb{R}^{d-1},\ t \in [0,T]. \quad (4)$$

3.2 Fourier diffraction theorem

Besides the convolutional representation (4), the forward map $\mathcal{D}^{\mathrm{tot}}$ may be represented using the Fourier transform, which significantly simplifies the inversion. The d-dimensional *Fourier transform* is defined by

$$\mathcal{F}[f](\boldsymbol{y}) := (2\pi)^{-d/2}\int_{\mathbb{R}^d} f(\boldsymbol{x})\,\mathrm{e}^{-\mathrm{i}\,\boldsymbol{x}\cdot\boldsymbol{y}}\,\mathrm{d}\boldsymbol{y}, \qquad \boldsymbol{y} \in \mathbb{R}^d, \quad (5)$$

and the *partial Fourier transform* with respect to the first $d-1$ coordinates by

$$\mathcal{F}_{1,\dots,d-1}[f](\boldsymbol{y}', x_d) := (2\pi)^{-(d-1)/2}\int_{\mathbb{R}^{d-1}} f(\boldsymbol{x}', x_d)\,\mathrm{e}^{-\mathrm{i}\,\boldsymbol{x}'\cdot\boldsymbol{y}'}\,\mathrm{d}\boldsymbol{x}' \quad (6)$$

for $(\boldsymbol{y}', x_d) \in \mathbb{R}^{d-1}\times\mathbb{R}$. Recalling that k_0 is the wave number of the incident field, we further define

$$\kappa(\boldsymbol{y}') := \sqrt{k_0^2 - \|\boldsymbol{y}'\|_2^2} \qquad \text{and} \qquad \boldsymbol{h}(\boldsymbol{y}') := \begin{pmatrix} \boldsymbol{y}' \\ \kappa(\boldsymbol{y}') - k_0 \end{pmatrix} \in \mathbb{R}^d.$$

where $\boldsymbol{y}' \in \mathcal{B}_{k_0}^{d-1}$. The *Fourier diffraction theorem* [45, 60] now states

$$\mathcal{F}_{1,\dots,d-1}[u_t^{\mathrm{sca}}](\boldsymbol{y}', r_{\mathrm{M}}) = \frac{\mathrm{i}\sqrt{\pi}}{\sqrt{2}\,\kappa(\boldsymbol{y}')}\,\mathrm{e}^{\mathrm{i}\,\kappa(\boldsymbol{y}')\,r_{\mathrm{M}}}\,\mathcal{F}[f](R_t\boldsymbol{h}(\boldsymbol{y}')), \qquad \boldsymbol{y}' \in \mathcal{B}_{k_0}^{d-1},\ t \in [0,T]. \quad (7)$$

In general, the identity (7) only holds in a distributional sense [48]. Geometrically, the set $\{\boldsymbol{h}(\boldsymbol{y}') : \|\boldsymbol{y}'\|_2 < k_0\}$ is a semisphere or semicircle, whose center is on the negative x_d axis, and which passes through the origin. On the right-hand side of (7), we thus evaluate the Fourier transform $\mathcal{F}[f]$ on a rotated semisphere or semicircle; on the left-hand side, partial Fourier transforms of the measurements $u_t^{\mathrm{sca}}(\cdot, r_{\mathrm{M}})$ are computed.

3.3 Uniqueness of the reconstruction

Under certain conditions, the scattering potential f is uniquely determined by the given measurements of u_t^{tot}. The following uniqueness result is based on the Paley–Wiener theorem [41, Thm. 7.3.1].

Proposition 3.1 (Paley–Wiener) *Let $f \in L^1(\mathbb{R}^d)$ have compact support. Then the Fourier transform $\mathcal{F}[f] \in C(\mathbb{R}^d)$ is uniquely extendable to an analytic function on $\mathbb{C}^d$.*

Theorem 3.2 (ODT inversion) *Let $f \in L^1(\mathbb{R}^d)$ have a compact support in $\mathcal{B}^d_{r_{\mathrm{M}}}$, and let the Lebesgue measure of*

$$\mathcal{Y} := \{R_t \boldsymbol{h}(\boldsymbol{y}') : \boldsymbol{y}' \in \mathcal{B}^{d-1}_{k_0},\, t \in [0,T]\} \subset \mathbb{R}^d \tag{8}$$

be positive. Then f is uniquely determined by $\mathcal{D}^{\mathrm{tot}}[f]$ in (4).

Proof: Given u_t^{tot}, we have $u_t^{\mathrm{sca}} = u_t^{\mathrm{tot}} - \mathrm{e}^{\mathrm{i}k_0 r_{\mathrm{M}}}$. By the Fourier diffraction theorem (7), we obtain $\mathcal{F}[f]$ on $\mathcal{Y}$, which has positive Lebesgue measure. Any d-variate analytic function is uniquely determined by its values on a set of positive Lebesgue measure [52, Sect. 4.1]. Since $\mathcal{F}[f]$ is an analytic function by Proposition 3.1, $\mathcal{F}[f]$ is uniquely determined on $\mathbb{R}^d$ and thus f itself due to the uniqueness of the Fourier transform [62, Thm. 4.47]. ▫

The requirements of Theorem 3.2 are, for instance, fulfilled if R_t describes a full rotation around an axis different from x_3 in 3D, or if the rotation angle covers an interval in 2D.

4 Discretization

The mapping $\mathcal{D}^{\mathrm{tot}}$ and its inversion can be numerically realized utilizing the Fourier diffraction theorem (7). For this purpose, we first restrict the total field u_t^{tot} or, more precisely, the scattered field u_t^{sca} to the cube $[-L_{\mathrm{M}}, L_{\mathrm{M}}]^{d-1}$ and then discretize the fields using $N \in 2\mathbb{N}$ samples for each spatial direction and $M \in \mathbb{N}$ time steps, cf. [48]. On the uniforms grids

$$\boldsymbol{z}'_{\boldsymbol{n}} := \tfrac{2L_{\mathrm{M}}}{N}\,\boldsymbol{n}, \quad \boldsymbol{n} \in \mathcal{I}_N^{d-1} \qquad \text{and} \qquad t_m := \tfrac{T}{M}\,m, \quad m \in \mathcal{J}_M, \tag{9}$$

the scattered fields $u_t^{\mathrm{sca}}(\boldsymbol{z}', r_{\mathrm{M}})$ are represented by the vectors

$$\boldsymbol{v}_m^{\mathrm{sca}} := \left[v_{m,\boldsymbol{n}}^{\mathrm{sca}}\right]_{\boldsymbol{n}\in\mathcal{I}_N^{d-1}} \qquad \text{with} \qquad \boldsymbol{v}_{m,\boldsymbol{n}}^{\mathrm{sca}} := u_{t_m}^{\mathrm{sca}}(\boldsymbol{z}'_{\boldsymbol{n}}, r_{\mathrm{M}}).$$

The $(d-1)$-dimensional *discrete Fourier transform* (DFT) of $\boldsymbol{v}_m^{\mathrm{sca}}$ is given by

$$\left[\boldsymbol{F}_{\mathrm{DFT}}\,\boldsymbol{v}_m^{\mathrm{sca}}\right]_{\boldsymbol{\ell}} := \sum_{\boldsymbol{n}\in\mathcal{I}_N^{d-1}} v_{m,\boldsymbol{n}}^{\mathrm{sca}}\,\mathrm{e}^{-2\pi\mathrm{i}\boldsymbol{n}\cdot\boldsymbol{\ell}/N}, \qquad \boldsymbol{\ell} \in \mathcal{I}_N^{d-1}, \tag{10}$$

and may be inverted using the inverse DFT

$$v^{\mathrm{sca}}_{m,\boldsymbol{n}} = \frac{1}{N^{d-1}} \sum_{\boldsymbol{\ell}\in\mathcal{I}_N^{d-1}} [\boldsymbol{F}_{\mathrm{DFT}}\, \boldsymbol{v}^{\mathrm{sca}}_m]_{\boldsymbol{\ell}}\, \mathrm{e}^{2\pi \mathrm{i} \boldsymbol{n}\cdot\boldsymbol{\ell}/N}, \qquad \boldsymbol{n}\in\mathcal{I}_N^{d-1}. \tag{11}$$

The left-hand side of the Fourier diffraction theorem (7) may thus be discretized as

$$\mathcal{F}_{1,\dots,d-1} u^{\mathrm{sca}}_{t_m}(\boldsymbol{y}'_{\boldsymbol{\ell}}, r_{\mathrm{M}}) \approx (2\pi)^{-\frac{d-1}{2}} \left(\tfrac{2L_{\mathrm{M}}}{N}\right)^{d-1} [\boldsymbol{F}_{\mathrm{DFT}}\, \boldsymbol{v}^{\mathrm{sca}}_m]_{\boldsymbol{\ell}}, \qquad \boldsymbol{\ell}\in\mathcal{I}_N^{d-1}, \tag{12}$$

where $\boldsymbol{y}'_{\boldsymbol{\ell}} := \frac{\pi}{L_{\mathrm{M}}}\boldsymbol{\ell}$ with $\boldsymbol{\ell}\in\mathcal{I}_N^{d-1}$, which provides an approximation of $\mathcal{F}[f]$ on the nonuniform grid

$$\mathcal{Y}_{M,N} := \left\{ R_{t_m}\boldsymbol{h}(\boldsymbol{y}'_{\boldsymbol{\ell}}) : m\in\mathcal{J}_M, \boldsymbol{\ell}\in\mathcal{I}_N^{d-1}, \|\boldsymbol{y}'_{\boldsymbol{\ell}}\| < k_0 \right\}. \tag{13}$$

For simplicity, we assume $\|\boldsymbol{y}'_{\boldsymbol{\ell}}\|_2 < k_0$ for all $\boldsymbol{\ell}\in\mathcal{I}_N^{d-1}$ and truncate the grid to the points satisfying this assumption.

For the right-hand side of the Fourier diffraction theorem, we assume $\operatorname{supp} f \subset [-L_{\mathrm{s}}, L_{\mathrm{s}}]^d$ and use $K\in 2\mathbb{N}$ sampling points per direction. Using the uniform grid

$$\boldsymbol{x}_{\boldsymbol{k}} := \tfrac{2L_{\mathrm{s}}}{K}\boldsymbol{k}, \qquad \boldsymbol{k}\in\mathcal{I}_K^d,$$

we approximate the scattering potential f by

$$\boldsymbol{f} = [f_{\boldsymbol{k}}]_{\boldsymbol{k}\in\mathcal{I}_K^d} := [f(\boldsymbol{x}_{\boldsymbol{k}})]_{\boldsymbol{k}\in\mathcal{I}_K^d} \in \mathbb{R}^{K^d}.$$

The d-dimensional *nonuniform discrete Fourier transform* (NDFT) of $\boldsymbol{f}$ onto the set $\mathcal{Y}_{M,N}$ is defined by

$$[\boldsymbol{F}_{\mathrm{NDFT}}\boldsymbol{f}]_{m,\boldsymbol{\ell}} := \sum_{\boldsymbol{k}\in\mathcal{I}_K^d} f_{\boldsymbol{k}}\, \mathrm{e}^{-\mathrm{i}\boldsymbol{x}_{\boldsymbol{k}}\cdot\left(R_{t_m}\boldsymbol{h}(\boldsymbol{y}'_{\boldsymbol{\ell}})\right)}, \qquad m\in\mathcal{J}_M,\ \boldsymbol{\ell}\in\mathcal{I}_N^{d-1}, \tag{14}$$

which approximates the right-hand Fourier transform in (7) via

$$\mathcal{F}[f]\left(R_{t_m}\boldsymbol{h}\left(\boldsymbol{y}'_{\boldsymbol{\ell}}\right)\right) \approx (2\pi)^{-\frac{d}{2}} \left(\frac{2L_{\mathrm{s}}}{K}\right)^d [\boldsymbol{F}_{\mathrm{NDFT}}\boldsymbol{f}]_{m,\boldsymbol{\ell}}, \qquad m\in\mathcal{J}_M, \boldsymbol{\ell}\in\mathcal{I}_N^{d-1}. \tag{15}$$

Inserting the approximations (12) and (15) into the Fourier diffraction theorem (7), we obtain

$$(2\pi)^{-\frac{d-1}{2}} \left(\frac{2L_{\mathrm{M}}}{N}\right)^{d-1} [\boldsymbol{F}_{\mathrm{DFT}}\boldsymbol{v}^{\mathrm{sca}}_m]_{\boldsymbol{\ell}} \approx \frac{\mathrm{i}\sqrt{\pi}}{\sqrt{2}\,\kappa(\boldsymbol{y}'_{\boldsymbol{\ell}})}\, \mathrm{e}^{\mathrm{i}\,\kappa(\boldsymbol{y}'_{\boldsymbol{\ell}})\, r_{\mathrm{M}}}\, (2\pi)^{-\frac{d}{2}} \left(\frac{2L_{\mathrm{s}}}{K}\right)^d [\boldsymbol{F}_{\mathrm{NDFT}}\boldsymbol{f}]_{m,\boldsymbol{\ell}}.$$

With the definition

$$\boldsymbol{c} = [c_{\boldsymbol{\ell}}]_{\boldsymbol{\ell}\in\mathcal{I}_N^{d-1}} \in \mathbb{R}^{N^{d-1}} \quad \text{with} \quad c_{\boldsymbol{\ell}} := \frac{\mathrm{i}}{\kappa(\boldsymbol{y}'_{\boldsymbol{\ell}})}\, \mathrm{e}^{\mathrm{i}\,\kappa(\boldsymbol{y}'_{\boldsymbol{\ell}})\, r_{\mathrm{M}}} \left(\frac{N}{L_{\mathrm{M}}}\right)^{d-1} \left(\frac{L_{\mathrm{s}}}{K}\right)^d,$$

the discrete Fourier diffraction theorem becomes

$$[\boldsymbol{F}_{\mathrm{DFT}}\boldsymbol{v}_m^{\mathrm{sca}}]_{\boldsymbol{\ell}} \approx c_{\boldsymbol{\ell}}\ (\boldsymbol{F}_{\mathrm{NDFT}}\boldsymbol{f})_{m,\boldsymbol{\ell}}\,.$$

Incorporating the incident field, we approximate $\mathcal{D}^{\mathrm{tot}}$ in (4) by the discrete diffraction tomography map

$$\boldsymbol{D}^{\mathrm{tot}}\boldsymbol{f} := \boldsymbol{F}_{\mathrm{DFT}}^{-1}(\boldsymbol{c}\odot\boldsymbol{F}_{\mathrm{NDFT}}\boldsymbol{f}) + \mathrm{e}^{\mathrm{i}k_0 r_{\mathrm{M}}}, \qquad \boldsymbol{f}\in\mathbb{R}^{K^d}, \tag{16}$$

where $\odot$ denotes the Hadamard (entrywise) product of two matrices or vectors. The numerical computation of the discrete forward transform $\boldsymbol{D}^{\mathrm{tot}}$ basically consists of an NDFT, an entrywise multiplication with $\boldsymbol{c}$, and a DFT, see Algorithm 1.

Algorithm 1: Computation of $\boldsymbol{D}^{\mathrm{tot}}$

Input: Scattering potential $\boldsymbol{f} = [f(\boldsymbol{x}_{\boldsymbol{k}})]_{\boldsymbol{k}\in\mathcal{I}_K^d}$.
Compute the NDFT $\boldsymbol{g} := \boldsymbol{F}_{\mathrm{NDFT}}\boldsymbol{f}$ by (14);
for $m\in\mathcal{J}_M$ **do**
  $\tilde{\boldsymbol{g}}_m := \boldsymbol{c}\odot\boldsymbol{g}_m$;
  $\boldsymbol{v}_m^{\mathrm{sca}} := \boldsymbol{F}_{\mathrm{DFT}}^{-1}\tilde{\boldsymbol{g}}_m$;
end
Output: Scattered wave $u_{t_m}^{\mathrm{tot}}\big(\boldsymbol{n}\frac{2L_{\mathrm{M}}}{N}, r_{\mathrm{M}}\big) \approx \boldsymbol{v}_{m,\boldsymbol{n}}^{\mathrm{sca}} + \mathrm{e}^{\mathrm{i}k_0 r_{\mathrm{M}}}$, $m\in\mathcal{J}_M$, $\boldsymbol{n}\in\mathcal{I}_N^{d-1}$.

The reconstruction of $\boldsymbol{f}$, see Algorithm 2, is basically an inverse of the forward transform. The first two parts are very simple to invert utilizing the DFT (11) and a pointwise division. However, the inversion of the NDFT is a more challenging problem that is covered in the following Section 5. A schematic overview about the reconstruction steps is provided in Figure 2.

Algorithm 2: Inversion of $\boldsymbol{D}^{\mathrm{tot}}$

Input: Scattered wave $\boldsymbol{v}_{m,\boldsymbol{n}}^{\mathrm{sca}} := u_{t_m}^{\mathrm{tot}}\big(\boldsymbol{n}\frac{2L_{\mathrm{M}}}{N}, r_{\mathrm{M}}\big) - \mathrm{e}^{\mathrm{i}k_0 r_{\mathrm{M}}}$, $m\in\mathcal{J}_M$, $\boldsymbol{n}\in\mathcal{I}_N^{d-1}$.
for $m\in\mathcal{J}_M$ **do**
  $\tilde{\boldsymbol{g}}_m := \boldsymbol{F}_{\mathrm{DFT}}\boldsymbol{v}_m^{\mathrm{sca}}$;
  $\boldsymbol{g}_m := \tilde{\boldsymbol{g}}_m \oslash \boldsymbol{c}$, where $\oslash$ denotes the Hadamard (entrywise) division;
end
Compute the inverse NDFT by solving $\boldsymbol{F}_{\mathrm{NDFT}}\boldsymbol{f} = \boldsymbol{g}$ for $\boldsymbol{f}$, see Section 5;
Output: Scattering potential $\boldsymbol{f} \approx [f(\boldsymbol{x}_{\boldsymbol{k}})]_{\boldsymbol{k}\in I_K^d}$.

The DFT (10) and its inverse (11) can be computed efficiently with the well-known *fast Fourier transform* (FFT) in $\mathcal{O}(N^{d-1}\log N)$ operations. Furthermore, there are fast algorithms for the computation of the NDFT (14) known as *nonuniform fast Fourier transform* (NFFT), which provides an arbitrarily tight approximation of the NDFT and uses $\mathcal{O}(K^d\log K)$ instead of the $\mathcal{O}(K^{2d})$ operations of the naive matrix-vector multiplication [9, 20, 64]. For our numerical simulations, we use the implementation of the

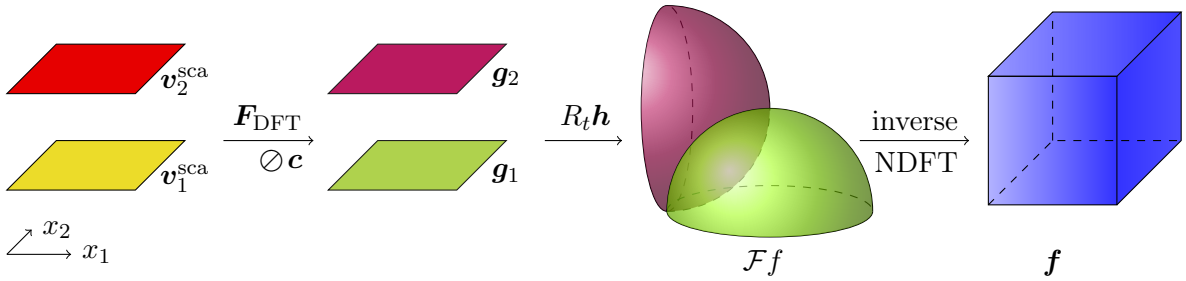

Figure 2: Schematic overview of the reconstruction process in 3D using Algorithm 2. We exemplarily use two rotations of angle 0 and $\pi/2$ around the x_2 axis. The first step consists of 2D DFTs along each layer of the data $\boldsymbol{v}^{\mathrm{sca}}$ and the division by $\boldsymbol{c}$. These functions are aligned on semispheres in the Fourier space according to the map $R_t\boldsymbol{h}$. Finally, $\boldsymbol{f}$ is recovered by a 3D inverse NDFT.

NFFT [47] provided in the software package [46], which also includes a fast algorithm for the adjoint NDFT with the same arithmetic complexity.

The NDFT (14) may also be interpreted as the (discretized) Fourier integral operator $g(\boldsymbol{\ell}, m) = \sum_{\boldsymbol{k}\in\mathcal{I}_K^d} \mathrm{e}^{\mathrm{i}\,\Phi((\boldsymbol{\ell},m),\boldsymbol{k})} f_{\boldsymbol{k}}$ with $\Phi((\boldsymbol{\ell}, m), \boldsymbol{k}) = -2L_{\mathrm{s}}K^{-1}\,(R_{t_m}\boldsymbol{h}(\boldsymbol{y}'_{\boldsymbol{\ell}}))\cdot\boldsymbol{k}$, such operators are more generally studied in [12]. This allows to apply fast butterfly algorithms [55], which are of the same asymptotic complexity as the NFFT.

5 Inverse NDFT as inverse problem

The approximate inversion of the NDFT (14) is the most crucial part for the reconstruction in Algorithm 2. Let $\boldsymbol{g} \in \mathbb{R}^{MN^{d-1}}$ be given. An (approximate) solution $\boldsymbol{f} \in \mathbb{R}^{K^d}$ of

$$\boldsymbol{F}_{\mathrm{NDFT}}\boldsymbol{f} = \boldsymbol{g} \tag{17}$$

is called an *inverse NDFT* of $\boldsymbol{g}$. There is no exact inversion formula known in general. Depending on the distribution of the nodes $\mathcal{Y}_{M,N}$, the inverse NDFT (17) might not have a unique solution or be ill-conditioned [62, Sect. 7.6.2].

5.1 Discrete backpropagation

The idea behind the backpropagation [19] is to apply a quadrature rule to the (continuous) inverse Fourier transform restricted to the set $\mathcal{Y}$ in (8), where values are available by the Fourier diffraction theorem (7). The *continuous backpropagation* is defined by

$$(2\pi)^{-d/2}\int_{\mathcal{Y}} \mathcal{F}[f](\boldsymbol{y})\,\mathrm{e}^{\mathrm{i}\,\boldsymbol{y}\cdot\boldsymbol{x}}\,\mathrm{d}\boldsymbol{y}, \qquad \boldsymbol{x}\in\mathbb{R}^d, \tag{18}$$

which is simply the inverse Fourier transform applied to $\mathbf{1}_{\mathcal{Y}}\mathcal{F}[f]$, where $\mathbf{1}_{\mathcal{Y}}(\boldsymbol{y}) \coloneqq 1$ if $\boldsymbol{y} \in \mathcal{Y}$ and zero elsewhere. Applying the substitution $(t, \boldsymbol{z}') \mapsto \boldsymbol{y} = R_t \boldsymbol{h}(\boldsymbol{z}')$ and a quadrature rule with nodes $(t_m, \boldsymbol{z}'_{\boldsymbol{n}})$ and weights $\boldsymbol{w} = [w_{m,\boldsymbol{n}}]_{m\in\mathcal{J}_M, \boldsymbol{n}\in\mathcal{I}_N^{d-1}} \in \mathbb{R}_{>0}^{MN^{d-1}}$ to (18), we arrive at the *discrete backpropagation (BP)* $\boldsymbol{B}$ of $\boldsymbol{g}$, namely

$$[\boldsymbol{B}\boldsymbol{g}]_{\boldsymbol{k}} \coloneqq \sum_{m\in\mathcal{J}_M} \sum_{\boldsymbol{n}\in\mathcal{I}_N^{d-1}} w_{m,\boldsymbol{n}}\, g_{m,\boldsymbol{n}}\, \mathrm{e}^{-\mathrm{i}\,(\boldsymbol{k}\frac{2L_{\mathrm{s}}}{K})\cdot(R_{t_m}\boldsymbol{h}(\boldsymbol{z}'_{\boldsymbol{n}}))}, \qquad \boldsymbol{k} \in \mathcal{I}_K^d. \tag{19}$$

For many situations in ODT, the weights $\boldsymbol{w}$ are known analytically [48, Sect. 4]. For instance, if the 3D object makes a full turn around the x_1 axis with rotation angle $t \in [0, 2\pi]$, we have the nodes (9) and weights

$$w_{m,\boldsymbol{n}} = \frac{k_0\,|[\boldsymbol{z}'_{\boldsymbol{n}}]_2|}{2\,\kappa(\boldsymbol{z}'_{\boldsymbol{n}})}\,\frac{2\pi^2 k_0^2}{MN^2}, \qquad m \in \mathcal{J}_M,\ \boldsymbol{n} \in \mathcal{I}_N^2. \tag{20}$$

The discrete backpropagation is an adjoint NDFT, i.e. $\boldsymbol{B}\boldsymbol{g} = \boldsymbol{F}_{\mathrm{NDFT}}^*(\boldsymbol{w} \odot \boldsymbol{g})$, which can be efficiently evaluated via the adjoint NFFT.

5.2 Conjugate gradient method

Equation (17) is a linear equation system that may be solved in the least-square sense by applying the iterative *conjugate gradient* (CG) method. This approach has been successfully applied in ODT [27, 48] as well as in X-ray imaging [63], magnetic resonance imaging [51], or spherical tomography [40]. We consider the overdetermined case $MN^{d-1} \geqslant K^d$. The underdetermined case is similar and covered in [54]. The idea is to

Algorithm 3: CG inversion of the NDFT

Input: $\boldsymbol{g} = [g_{m,\boldsymbol{n}}]_{m\in\mathcal{J}_M,\boldsymbol{n}\in\mathcal{I}_N} \in \mathbb{C}^{MN^{d-1}}$, $\boldsymbol{w} \in \mathbb{R}_{>0}^{MN^{d-1}}$, $\boldsymbol{f}^{(0)} \in \mathbb{R}^{K^d}$, $J_{\mathrm{CG}} \in \mathbb{N}$.

$\boldsymbol{r}^{(0)} \coloneqq \boldsymbol{g}$;

$\boldsymbol{p}^{(0)} \coloneqq \boldsymbol{s}^{(0)} \coloneqq \mathrm{Re}[\boldsymbol{F}_{\mathrm{NDFT}}^*(w \odot \boldsymbol{r}^{(0)})]$;

for $j = 0, 1, \ldots, J_{\mathrm{CG}}$ **do**

- $\boldsymbol{q}^{(j)} \coloneqq \boldsymbol{F}_{\mathrm{NDFT}}\boldsymbol{p}^{(j)}$;
- $\alpha_j \coloneqq (\boldsymbol{s}^{(j)})^*\,\boldsymbol{s}^{(j)} / (\boldsymbol{q}^{(j)})^*\,(\boldsymbol{w} \odot \boldsymbol{q}^{(j)})$;
- $\boldsymbol{f}^{(j+1)} \coloneqq \boldsymbol{f}^{(j)} + \alpha_j\,\boldsymbol{p}^{(j)}$;
- $\boldsymbol{r}^{(j+1)} \coloneqq \boldsymbol{r}^{(j)} - \alpha_j\,\boldsymbol{q}^{(j)}$;
- $\boldsymbol{s}^{(j+1)} \coloneqq \mathrm{Re}[\boldsymbol{F}_{\mathrm{NDFT}}^*(\boldsymbol{w} \odot \boldsymbol{r}^{(j+1)})]$;
- $\beta_j \coloneqq (\boldsymbol{s}^{(j+1)})^*\,\boldsymbol{s}^{(j+1)} / (\boldsymbol{s}^{(j)})^*\,\boldsymbol{s}^{(j)}$;
- $\boldsymbol{p}^{(j+1)} \coloneqq \boldsymbol{s}^{(j+1)} + \beta_j\,\boldsymbol{p}^{(j+1)}$;

end

Output: Approximate solution $\boldsymbol{f}^{(J_{\mathrm{CG}})} \in \mathbb{R}^{K^d}$.

find a solution $\boldsymbol{f} \in \mathbb{R}^{K^d}$ of

$$\underset{\boldsymbol{f}\in\mathbb{R}^{K^d}}{\text{minimize}} \qquad \|\boldsymbol{F}_{\text{NDFT}}\boldsymbol{f} - \boldsymbol{g}\|_{2,\boldsymbol{w}}^2 \tag{21}$$

with some weights $\boldsymbol{w} = [w_{m,\boldsymbol{n}}]_{m\in\mathcal{J}_M,\boldsymbol{n}\in\mathcal{I}_N^{d-1}} \in \mathbb{R}_{>0}^{MN^{d-1}}$. The classical CG method corresponds to the constant weights $w_{m,\boldsymbol{n}} \equiv 1$. Obviously, any exact solution $\boldsymbol{f}$ of (17) is a minimizer of (21). We apply the CG method on the normal equation

$$\operatorname{Re}[\boldsymbol{F}_{\text{NDFT}}^*(\boldsymbol{w} \odot \boldsymbol{F}_{\text{NDFT}}\boldsymbol{f})] = \operatorname{Re}[\boldsymbol{F}_{\text{NDFT}}^*(\boldsymbol{w} \odot \boldsymbol{g})],$$

where $\boldsymbol{f}$ is assumed to be real-valued. This approach results in Algorithm 3, which is known as CGNE (CG on the normal equations), CGNR (CG minimizing the norm of the residual) or CGLS (CG minimizing least squares). The iterative method requires the evaluation of $\boldsymbol{F}_{\text{NDFT}}$ and $\boldsymbol{F}_{\text{NDFT}}^*$ in each iteration. For a more detailed description of the algorithm, we refer to [38, 51].

Good weights $\boldsymbol{w}$ ensure that $\boldsymbol{F}_{\text{NDFT}}^*(\boldsymbol{w} \odot \boldsymbol{g})$ is close to the desired solution $\boldsymbol{f}$. In this case, the CG usually converges faster. One possibility to choose $\boldsymbol{w}$ are the quadrature weights (20) with respect to $\mathcal{Y}_{M,N}$ [51]. The CG algorithm is a simple regularization method, where the number of iterations acts as regularization parameter [23, Sect. 7].

5.3 Total variation regularization

In order to stabilize the inversion of the NDFT, we regularize (17) by the total variation (TV) semi-norm. For a discrete image $\boldsymbol{f} \in \mathbb{R}^{K^d}$, the *total variation* becomes

$$\operatorname{TV}(\boldsymbol{f}) := \sum_{\boldsymbol{k}\in\mathcal{I}_K^d} \|(\operatorname{grad}\boldsymbol{f})_{\boldsymbol{k}}\|_2 = \|\operatorname{grad}\boldsymbol{f}\|_{1,2},$$

see for instance Bredies & Lorenz [11], where the discrete gradient $\operatorname{grad}\colon \mathbb{R}^{K^d} \to \mathbb{R}^{K^d\times d}$ yields a discrete vector field by applying the finite forward differences with respect to each axis. More precisely, the discrete gradient is defined by

$$(\operatorname{grad}\boldsymbol{f})_{\boldsymbol{k},\ell} = (\partial_\ell \boldsymbol{f})_{\boldsymbol{k}} \qquad \text{with} \qquad (\partial_\ell \boldsymbol{f})_{\boldsymbol{k}} := \begin{cases} f_{\boldsymbol{k}+\boldsymbol{e}_\ell} - f_{\boldsymbol{k}}, & k_\ell < \frac{K}{2} - 1, \\ 0, & k_\ell = \frac{K}{2} - 1, \end{cases} \tag{22}$$

for $\boldsymbol{k} \in \mathcal{I}_K^d$ and $\ell \in \mathcal{J}_d$, where $\boldsymbol{e}_\ell$ corresponds to the ℓth unit vector. The adjoint of the discrete gradient is the negative discrete divergence, i.e. $\operatorname{grad}^* = -\operatorname{div}$. Using finite backward differences, we define the discrete divergence by

$$\operatorname{div}\boldsymbol{y} := \sum_{\ell=1}^{d} \tilde{\partial}_\ell \boldsymbol{y}_{\cdot,\ell} \qquad \text{with} \qquad (\tilde{\partial}_\ell \boldsymbol{f})_{\boldsymbol{k}} := \begin{cases} f_{\boldsymbol{k}}, & k_\ell = -\frac{K}{2}, \\ f_{\boldsymbol{k}} - f_{\boldsymbol{k}-\boldsymbol{e}_\ell}, & -\frac{K}{2} < k_\ell < \frac{K}{2} - 1, \\ -f_{\boldsymbol{k}-\boldsymbol{e}_\ell}, & k_\ell = \frac{K}{2} - 1, \end{cases}$$

where $\boldsymbol{y}_{\cdot,\ell}$ denotes the ℓth components of the discrete vector field $\boldsymbol{y} \in \mathbb{R}^{K^d \times d}$.

The TV regularization is well known to promote cartoon-like images such as the objects we expect in our specific application. Besides this a priori information, we know that the images representing the physical object are real-valued and non-negative. Incorporating this knowledge, we propose to compute the NDFT by minimizing the variational formulation

$$\underset{\boldsymbol{f}\in\mathbb{R}^{K^d}}{\text{minimize}} \qquad \underbrace{\chi_{\mathbb{R}^{K^d}_{\geqslant 0}}(\boldsymbol{f})}_{=:F(\boldsymbol{f})} + \underbrace{\tfrac{1}{2}\|\boldsymbol{F}_{\text{NDFT}}(\boldsymbol{f}) - \boldsymbol{g}\|^2_{2,\boldsymbol{w}}}_{=:G(\boldsymbol{f})} + \underbrace{\lambda\|\operatorname{grad}\boldsymbol{f}\|_{1,2}}_{=:H(L\boldsymbol{f})}, \tag{23}$$

where $L := \operatorname{grad}$ and $\chi_{\mathbb{R}^{K^d}_{\geqslant 0}}$ is the characteristic function over the non-negative orthant given by

$$\chi_{\mathbb{R}^{K^d}_{\geqslant 0}}(\boldsymbol{f}) := \begin{cases} 0, & \text{if } f_{\boldsymbol{k}} \geqslant 0 \text{ for all } k \in \mathcal{I}^d_K, \\ +\infty, & \text{otherwise.} \end{cases}$$

A convex minimization problem like (23) may be numerically solved with the primal-dual (PD) iteration by Chambolle & Pock [15], which consists in

$$\begin{aligned} \boldsymbol{f}^{(j+1)} &:= \operatorname{prox}_{\tau F}\big(\boldsymbol{f}^{(j)} - \tau(\nabla G(\boldsymbol{f}^{(j)}) + L^*\boldsymbol{y}^{(j)})\big), \\ \boldsymbol{y}^{(j+1)} &:= \operatorname{prox}_{\sigma H^*}\big(\boldsymbol{y}^{(j)} + \sigma L(2\boldsymbol{f}^{(j+1)} - \boldsymbol{f}^{(j)})\big) \end{aligned}$$

for appropriate $\tau, \sigma > 0$. Here, ∇G denotes the gradient of the differentiable function G in contrast to the discrete gradient (22) of a multidimensional signal. More generally, the *proximal mapping* of a convex function $h\colon \mathbb{R}^K \to \mathbb{R} \cup \{-\infty, +\infty\}$ is defined by

$$\operatorname{prox}_h(\boldsymbol{x}) := \underset{\boldsymbol{y}\in\mathbb{R}^K}{\arg\min}\, h(\boldsymbol{y}) + \tfrac{1}{2}\,\|\boldsymbol{x} - \boldsymbol{y}\|^2_2. \tag{24}$$

If h is additionally proper, i.e. not everywhere $+\infty$ and never $-\infty$, and lower semi-continuous, then the minimizer in (24) is unique, and the proximal mapping becomes single valued. Further, the *Fenchel* or *convex conjugate* of the convex function h is defined by

$$h^*(\boldsymbol{x}) := \sup_{\boldsymbol{y}\in\mathbb{R}^K} \langle \boldsymbol{x}, \boldsymbol{y}\rangle - h(\boldsymbol{y}).$$

Since the proximal mapping of an indicator function is the projection to its support [4, Thm. 3.14], i.e.

$$\operatorname{prox}_{\mathbb{R}^{K^d}_{\geqslant 0}}(\boldsymbol{x}) = \operatorname{proj}_{\mathbb{R}^{K^d}_{\geqslant 0}}(\boldsymbol{x}) := \underset{\boldsymbol{y}\in\mathbb{R}^{K^d}_{\geqslant 0}}{\arg\min} \|\boldsymbol{x} - \boldsymbol{y}\|^2_2,$$

for our specific formulation (23), the PD iteration becomes

$$\begin{aligned} \boldsymbol{f}^{(j+1)} &:= \operatorname{proj}_{\mathbb{R}^{K^d}_{\geqslant 0}}(\boldsymbol{f}^{(j)} - \tau(\operatorname{Re}[\boldsymbol{F}^*_{\text{NDFT}}(\boldsymbol{w} \odot (\boldsymbol{F}_{\text{NDFT}}\boldsymbol{f}^{(j)} - \boldsymbol{g}))] - \operatorname{div}\boldsymbol{y}^{(j)})), \\ \boldsymbol{y}^{(j+1)} &:= \operatorname{prox}_{\sigma\lambda\|\cdot\|^*_{1,2}}(\boldsymbol{y}^{(j)} + \sigma\operatorname{grad}(2\boldsymbol{f}^{(j+1)} - \boldsymbol{f}^{(j)})). \end{aligned} \tag{25}$$

The remaining proximal mapping of the discrete TV semi-norm may be computed by exploiting

$$\operatorname{prox}_{\sigma\lambda\|\cdot\|_{1,2}^*}(\boldsymbol{y}) = \boldsymbol{y} - \sigma \operatorname{prox}_{\frac{\lambda}{\sigma}\|\cdot\|_{1,2}}(\tfrac{1}{\sigma}\boldsymbol{y}),$$

cf. [4, Thm. 14.3], and

$$(\operatorname{prox}_{\rho\|\cdot\|_{1,2}}(\boldsymbol{y}))_{\boldsymbol{k},\ell} = \big(1 - \tfrac{\rho}{\max\{\|\boldsymbol{y}_{\boldsymbol{k},\cdot}\|_2, \rho\}}\big)\, y_{\boldsymbol{k},\ell}$$

for some $\rho > 0$, see for example [17] and references therein.

The central pitfall of applying the PD iteration in practice is the selection of appropriate primal and dual step sizes τ and σ. In the literature, there exist several approaches to choose the step sizes adaptively [34, 68]. In our numerical experiments, we rely on the step size rules proposed in [68], which have been successfully applied to TV denoising in image processing. The main idea is to compute the primal and dual residuals

$$\begin{aligned}
\boldsymbol{p}^{(j+1)} &:= \tfrac{1}{\tau}\,(\boldsymbol{f}^{(j)} - \boldsymbol{f}^{(j+1)}) - \operatorname{Re}[\boldsymbol{F}_{\mathrm{NDFT}}^*(\boldsymbol{w} \odot \boldsymbol{F}_{\mathrm{NDFT}}(\boldsymbol{f}^{(j)} - \boldsymbol{f}^{(j+1)}))] + \operatorname{div}(\boldsymbol{y}^{(j)} - \boldsymbol{y}^{(j+1)}),\\
\boldsymbol{d}^{(j+1)} &:= \tfrac{1}{\sigma}\,(\boldsymbol{y}^{(j)} - \boldsymbol{y}^{(j+1)}) - \operatorname{grad}(\boldsymbol{f}^{(j)} - \boldsymbol{f}^{(j+1)}),
\end{aligned} \tag{26}$$

where we added the residual with respect to the gradient ∇G. Further, we require the values

$$\begin{aligned}
\alpha^{(j+1)} &:= \tfrac{\|\boldsymbol{f}^{(j+1)}\|_2}{\|\boldsymbol{y}^{(j+1)}\|_{2,2}},\\
\omega_{\mathrm{P}}^{(j+1)} &:= \frac{\langle \boldsymbol{f}^{(j)} - \boldsymbol{f}^{(j+1)}, \boldsymbol{p}^{(j+1)}\rangle}{\|\boldsymbol{f}^{(j)} - \boldsymbol{f}^{(j+1)}\|_2 \|\boldsymbol{p}^{(j+1)}\|_2},\\
\omega_{\mathrm{D}}^{(j+1)} &:= \frac{\langle \boldsymbol{y}^{(j)} - \boldsymbol{y}^{(j+1)}, \boldsymbol{d}^{(j+1)}\rangle}{\|\boldsymbol{y}^{(j)} - \boldsymbol{y}^{(j+1)}\|_{2,2} \|\boldsymbol{d}^{(j+1)}\|_{2,2}},
\end{aligned} \tag{27}$$

where the occurring inner products are defined via

$$\langle \boldsymbol{f}, \boldsymbol{g}\rangle := \sum_{\boldsymbol{k}\in\mathcal{I}_K^d} f_{\boldsymbol{k}} g_{\boldsymbol{k}} \qquad \text{and} \qquad \langle \boldsymbol{y}, \boldsymbol{z}\rangle := \sum_{\boldsymbol{k}\in\mathcal{I}_K^d} \langle \boldsymbol{y}_{\boldsymbol{k},\cdot}, \boldsymbol{z}_{\boldsymbol{k},\cdot}\rangle.$$

Now, if $\boldsymbol{f}^{(j)} - \boldsymbol{f}^{(j+1)}$ is aligned with primal residual $\boldsymbol{p}^{(j+1)}$, we increase the primal step size τ; and if $\boldsymbol{f}^{(j)} - \boldsymbol{f}^{(j+1)}$ is opposed to $\boldsymbol{p}^{(j+1)}$, we decrease τ. We proceed analogously for the dual step size σ. On the basis of the observation that a large τ and a small σ decrease the primal residual at the cost of the dual residual [34], Yokata & Hontani [68] propose to balance both step sizes by multiplying τ with a power of $\alpha^{(j+1)}$ and dividing σ by the same power of $\alpha^{(j+1)}$, which is greater than one if the primal residual dominates; or less than one if the dual residual dominates. Summarized, we apply the PD iteration with the parameter updates in Algorithm 4, which we call the PD method (with TV) for ODT. A more detailed motivation behind the acceleration, backtracking and balancing of the step sizes may be found in [68].

Algorithm 4: PD inversion of the NDFT with TV

Input: $\boldsymbol{g} = \boldsymbol{F}_{\mathrm{NDFT}}\boldsymbol{f}$, $\boldsymbol{w} \in \mathbb{R}_{>0}^{MN^{d-1}}$, $\lambda > 0$, $\boldsymbol{f}^{(0)} \in \mathbb{R}_{\geqslant 0}^{K^d}$, $\boldsymbol{y}^{(0)} \in \mathbb{R}^{K^d \times d}$, $\tau^{(0)} > 0$, $\sigma^{(0)} > 0$, $\rho = 0.005$, $c = 0.9$, $\beta = 1.5$, $\zeta = 0.25$, $J_{\mathrm{PD}} \in \mathbb{N}$.

for $j = 0, 1, 2, \ldots, J_{\mathrm{PD}}$ **do**

- Compute $\boldsymbol{f}^{(j+1)}$, $\boldsymbol{y}^{(j+1)}$ by (25);
- Compute $\boldsymbol{p}^{(j+1)}$, $\boldsymbol{d}^{(j+1)}$ by (26);
- Compute $\alpha^{(j+1)}$, $\omega_{\mathrm{P}}^{(j+1)}$, $\omega_{\mathrm{D}}^{(j+1)}$ by (27);
- **if** $\omega_{\mathrm{P}}^{(j+1)} > c$ **then** $\tau^{(j)} := \beta\tau^{(j)}$;
- **if** $\omega_{\mathrm{P}}^{(j+1)} < 0$ **then** $\tau^{(j)} := \zeta\tau^{(j)}$;
- **if** $\omega_{\mathrm{D}}^{(j+1)} > c$ **then** $\sigma^{(j)} := \beta\sigma^{(j)}$;
- **if** $\omega_{\mathrm{D}}^{(j+1)} < 0$ **then** $\sigma^{(j)} := \zeta\sigma^{(j)}$;
- Balancing: $\tau^{(j+1)} := (\alpha^{(j+1)})^{\rho}\tau^{(j)}$, $\sigma^{(j+1)} := \sigma^{(j)}/(\alpha^{(j+1)})^{\rho}$;

end

Output: Approximate scattering potential $\boldsymbol{f}^{(J_{\mathrm{PD}})}$.

5.4 Numerical backward transform

We numerically compare the three reconstruction approaches based on Algorithm 2, where the inverse NDFT step is realized via

i) the BP method (19),

ii) the CG method in Algorithm 3, and

iii) the PD method with TV in Algorithm 4.

Additionally, we apply TV denoising to the reconstructed images of i) and ii). The *TV denoising* (TVd) corresponds to finding a minimizer of

$$\underset{\tilde{\boldsymbol{f}} \in \mathbb{R}^{K^d}}{\text{minimize}} \qquad \chi_{\mathbb{R}_{\geqslant 0}^{K^d}}(\tilde{\boldsymbol{f}}) + \tfrac{1}{2}\,\|\tilde{\boldsymbol{f}} - \boldsymbol{f}\|_2^2 + \lambda\,\|\mathrm{grad}\,\tilde{\boldsymbol{f}}\|_{1,2}\,,$$

i.e., (23) with the identity instead of $\boldsymbol{F}_{\mathrm{NDFT}}$. In order to avoid the so-called "inverse crime," we compute the data via a direct discretization of the convolution (3). For some of the tests, we also disturb the measurements by additive noise; so in this case we have only access to $\boldsymbol{D}^{\mathrm{tot}}\boldsymbol{f} + \boldsymbol{\varepsilon}$ with $\boldsymbol{\varepsilon} \in \mathbb{C}^{MN^{d-1}}$ corresponding to the noise level $\|\boldsymbol{\varepsilon}\|_2 \,/\, \|\boldsymbol{D}^{\mathrm{tot}}\boldsymbol{f}\|_2$.

All numerical tests were performed on a standard PC with an 8-core Intel Core i7-10700 and 32 GB memory using Matlab with the NFFT library [46]. Our code is available in the `FourierODT` toolbox.[1] We compare the reconstruction quality by means of the

[1] https://github.com/michaelquellmalz/FourierODT

structural similarity index measure (SSIM) [66] and the *peak signal-to-noise ratio*

$$\mathrm{PSNR}(\boldsymbol{f},\boldsymbol{g}) := 10\log_{10}\frac{\max_{\boldsymbol{r}\in\mathcal{I}_K^d}|f_{\boldsymbol{k}}|^2}{K^{-d}\sum_{\boldsymbol{k}\in\mathcal{I}_K^d}|f_{\boldsymbol{k}}-g_{\boldsymbol{k}}|^2}, \qquad \boldsymbol{f},\boldsymbol{g}\in\mathbb{R}^{K^d}.$$

Two-dimensional function. For a 2D simulation, we employ the discretization parameters $K = N = M = 240$ as well as $r_{\mathrm{M}} = 40$ and $L_{\mathrm{M}} = 60$. We choose $L_{\mathrm{s}} = K/(4\sqrt{2}) \approx 42$, which ensures that $\mathcal{Y}_{\mathcal{M},\mathcal{N}}$ is inside one peridicity interval of the NDFT. We fix the wave number $k_0 = 2\pi$, which means that all spatial measurements are in multiples of the wavelength of the incident field u^{inc}. The object rotates a full turn around the center. The object $\boldsymbol{f}$ consists of different convex and concave shapes, see Figure 4a. The discrete sinogram $\boldsymbol{D}^{\mathrm{tot}}\boldsymbol{f}$ and the Fourier space data approximating $\mathcal{F}[f]$ on the set (13), which is contained in a disk of radius $\sqrt{2}\,k_0$, are shown in Figure 3.

	BP	BP & TVd	CG	CG & TVd	PD
PSNR	31.22	36.17	39.61	40.12	41.59
SSIM	0.388	0.991	0.983	0.990	0.988
Time (sec)	0.01	0.12	0.18	0.12	0.28

Table 1: Error for the reconstruction of the function of Figure 4a with exact data.

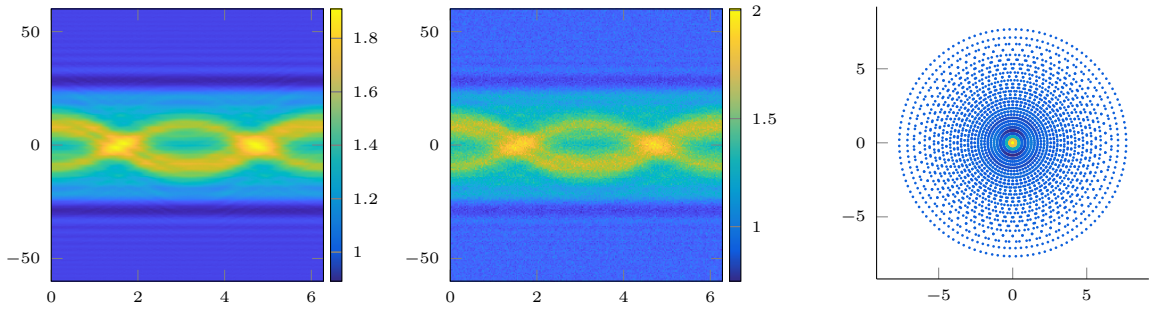

(a) Sinogram $\left|u_t^{\mathrm{tot}}(x)\right|$ for the function of Figure 4a

(b) Sinogram with 5 % Gaussian white noise

(c) Fourier space data on $\mathcal{Y}_{M,N}$ for a full turn

Figure 3: Visualization of the data and the respective Fourier space coverage.

For the reconstructions, we use $J_{\mathrm{CG}} = 20$ iterations for CG in Algorithm 3 and $J_{\mathrm{PD}} = 50$ iterations for PD with TV in Algorithm 4. Note that the BP and the CG reconstruction only assume that $\boldsymbol{f}$ is real-valued, whereas PD with TV incorporates the non-negativity of $\boldsymbol{f}$. The reconstruction error for exact data and the computation times are shown in Table 1 (all reconstructions look very good and are visually almost indistinguishable). Figure 4 shows the reconstructions for 5% complex Gaussian noise. Different from above, the CG method is performed with $J_{\mathrm{CG}} = 5$ iterations, which acts as regularization against the noise. The advantage of the TV regularization is clearly visible.

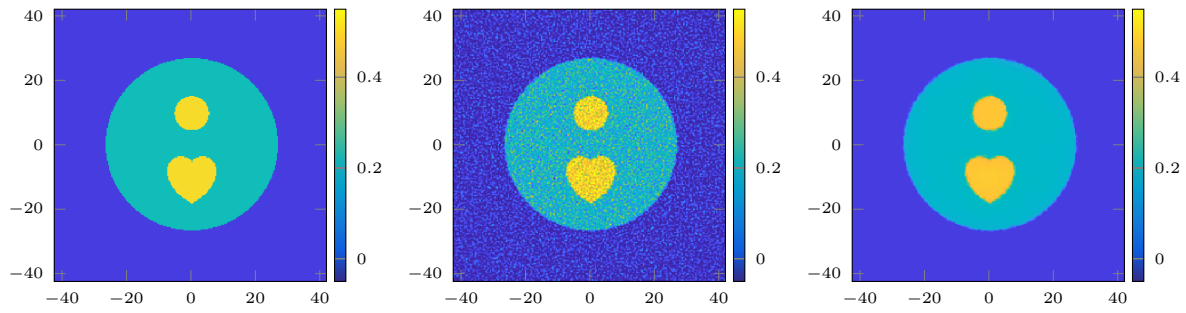

(a) Ground truth $\boldsymbol{f}$ (b) BP reconstruction PSNR 23.38, SSIM 0.125 (c) BP and TVd ($\lambda = 0.1$) PSNR 34.71, SSIM 0.985

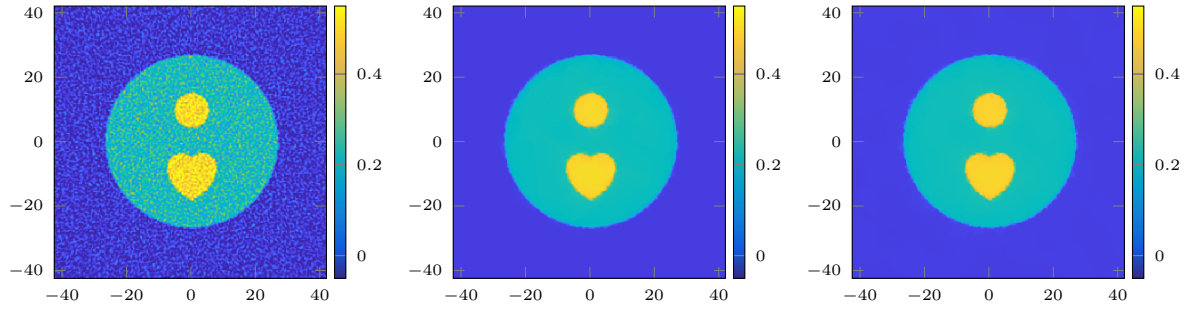

(d) CG reconstruction PSNR 26.03, SSIM 0.234 (e) CG and TVd ($\lambda = 0.1$) PSNR 38.05, SSIM 0.983 (f) PD with TV ($\lambda = 0.1$) PSNR 37.62, SSIM 0.872

Figure 4: Inversion of $\boldsymbol{D}^{\text{tot}}\boldsymbol{f}$ with 5% Gaussian noise using BP in (19), CG in Alg. 3, and PD with TV in Alg. 4. The BP and CG results are TV-denoised.

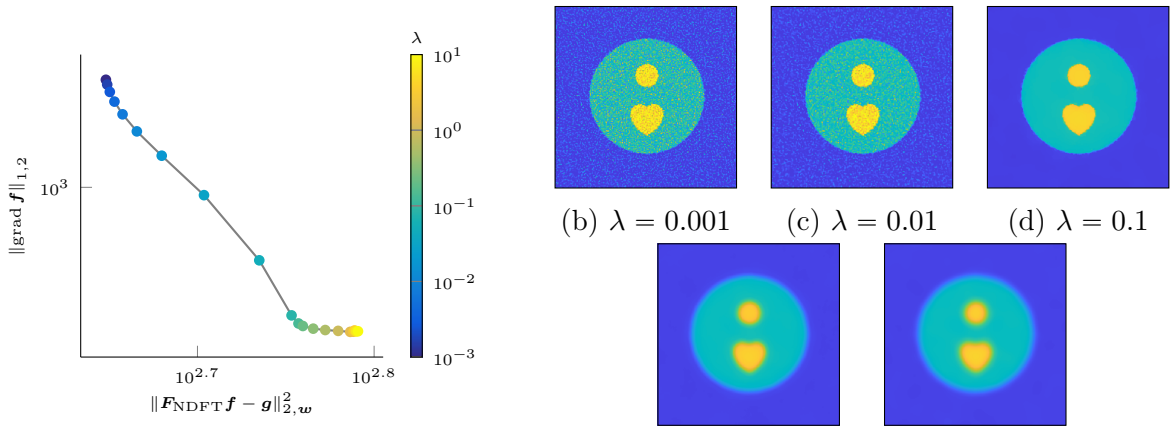

(a) L-curve (b) $\lambda = 0.001$ (c) $\lambda = 0.01$ (d) $\lambda = 0.1$ (e) $\lambda = 1$ (f) $\lambda = 10$

Figure 5: L-curve for the PD with TV in Figure 4f for $\lambda \in [10^{-3}, 10]$.

Instead of choosing an appropriate λ for PD with TV by hand as in the above simulations, different choice strategies may be applied [23, Sect. 4]. We obtained promising results with the L-curve method [39], which does not require a priori knowledge of the noise level. This method consists of choosing λ with respect to the "tip" of an L-shaped curve in a bilogarithmic plot of the residual $\|\boldsymbol{F}_{\mathrm{NDFT}}\boldsymbol{f}_\lambda - \boldsymbol{g}\|_{2,\boldsymbol{w}}^2$ versus the regularization $\|\mathrm{grad}\,\boldsymbol{f}_\lambda\|_{1,2}$ for varying λ, where $\boldsymbol{f}_\lambda$ denotes the reconstruction for a specific λ, and where $\boldsymbol{g}$ is computed form the data $\boldsymbol{v}_m^{\mathrm{sca}}$ as in Algorithm 2. An exemplary L-curve is displayed in Figure 5, where we can spot the "tip" around $\lambda \approx 0.1$. A second, much weaker kink at the top left around $\lambda \approx 0.01$ can be easily ruled out as the corresponding reconstruction $\boldsymbol{f}_\lambda$ looks very noisy.

Three-dimensional function. Our three-dimensional phantom contains a variety of shapes with smooth and non-smooth boundaries, see Figure 7a. The discretization parameters are the same as before. The object makes a full turn around the x_2 axis with the rotation angle $t \in [0, 2\pi]$. The measurements with respect to one illumination angle is shown in Figure 6. The respective Fourier space coverage $\mathcal{Y}$ in (8) has the form of a horn torus and is depicted in Figure 6c, cf. [48]. The so-called *missing cone* around the x_2 axis in the Fourier space coverage makes the reconstruction more difficult and promotes certain artifacts, like horizontal stripes at the top and bottom in Figure 7.

	BP	BP & TVd	CG	CG & TVd	PD
PSNR	29.07	32.79	33.36	33.82	34.36
SSIM	0.614	0.987	0.955	0.988	0.957
Time (sec)	4	31	79	31	1395

Table 2: Error for the reconstruction of the function of Figure 7a with exact data.

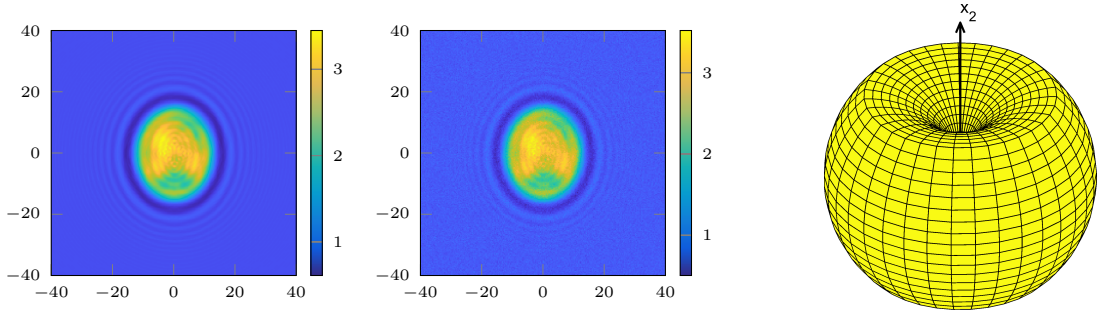

(a) Exact data. (b) Data with 5 % Gaussian noise. (c) Fourier space coverage $\mathcal{Y}$ for a full turn around the x_2 axis.

Figure 6: Data $|u_t^{\mathrm{tot}}(\cdot, r_{\mathrm{M}})|$ for the function of Figure 7a at one fixed time step t and the Fourier coverage $\mathcal{Y}$ in 3D.

The errors for exact data and computation times are presented in Table 2. The reconstructions with noisy data are shown in Figure 7. The CG reconstruction is again of

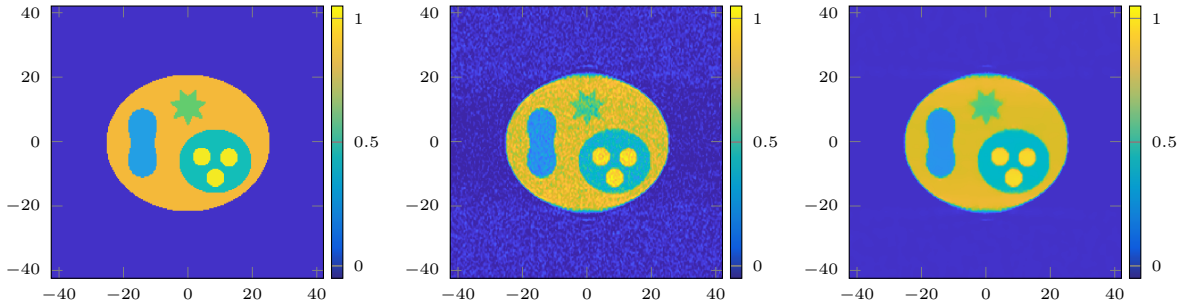

(a) Ground truth $\boldsymbol{f}$

(b) BP reconstruction
PSNR 24.53, SSIM 0.178

(c) BP and TVd ($\lambda = 0.05$)
PSNR 32.51, SSIM 0.968

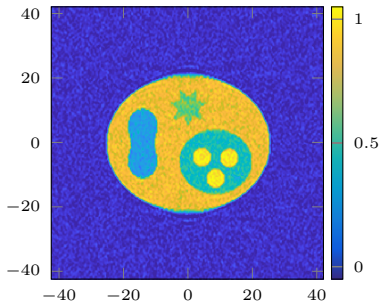

(d) CG Reconstruction
PSNR 26.74, SSIM 0.309

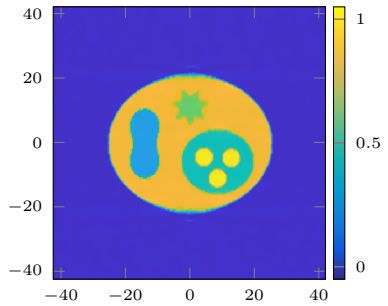

(e) CG and TVd ($\lambda = 0.02$)
PSNR 33.53, SSIM 0.965

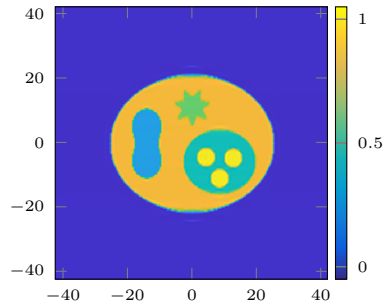

(f) PD with TV ($\lambda = 0.02$)
PSNR 33.58, SSIM 0.736

Figure 7: Slice $x_3 = 0.35$ of the 3D reconstruction from data with 5 % Gaussian noise using BP in (19), CG in Alg. 3, and PD with TV in Alg. 4.

better quality than BP. Both, however, contain visible noise, which is compensated in the additional TV denoising performed afterwards, where we make $J_{\mathrm{PD}} = 20$ iterations. Performing more iterations does not benefit the image quality significantly. The PD method with TV for the full inverse problem produces also a very good 3D reconstruction. However, the latter requires significantly more time since the primal-dual iteration converges rather slowly and requires $J_{\mathrm{PD}} = 100$ iterations to obtain a satisfying result. Furthermore, we notice that TV regularization may lead to staircasing [43] if the image is not piecewise constant. This phenomenon might be prevented by using higher-order generalizations of the total variation, see [10].

6 Phase retrieval in ODT

Different from the numerical experiments in Section 5.4, the phase of the complex diffraction patterns u_t^{tot} is usually unknown in practice. In other words, only the intensity $|u_t^{\mathrm{tot}}(\cdot, r_{\mathrm{M}})|$ is recorded. Due to the phase loss, the already ill-posed recovery problem is further hampered.

The numerical retrieval of an unknown phase traces back to the famous Gerchberg–Saxton algorithm [33], which was originally invented to capture a complex-valued object from its intensities in spatial and Fourier domain and was modified by Fienup [29] to recover an object from the modulus of its Fourier transform. The basic idea of Fienup's error-reduction algorithm is to enforce known object constraints in object domain and known magnitude constraints given by the data in Fourier domain alternatingly. The error-reduction algorithm is a specific version of more general input-output algorithms, which may be read as Algorithm 5, where $\boldsymbol{D}$ is a map modeling the measurement process, and where the sign function

$$\operatorname{sgn}(z) := \begin{cases} z/|z|, & z \in \mathbb{C}\backslash\{0\}, \\ 1, & z = 0, \end{cases}$$

is applied element by element. The error-reduction algorithm and modifications of it are nowadays still well-established approaches to solve phase retrieval problems in practice.

Algorithm 5: General input-output algorithm

Input: $\boldsymbol{d} = |\boldsymbol{D}(\boldsymbol{f})|$.
Initialize $\boldsymbol{g}^{(0)} := \boldsymbol{d}$;
for $j = 0, 1, 2, \dots, J_{\mathrm{IO}}$ **do**
  $\boldsymbol{f}^{(j)} := \boldsymbol{D}^{-1}\boldsymbol{g}^{(j)}$, see Algorithm 2;
  Set $\boldsymbol{f}^{(j+1/2)}$ by applying object domain constraints on $\boldsymbol{f}^{(j)}$ via (28) or (29);
  $\boldsymbol{g}^{(j+1/2)} := \boldsymbol{D}\boldsymbol{f}^{(j+1/2)}$, see Algorithm 1;
  $\boldsymbol{g}^{(j+1)} := \boldsymbol{d}\operatorname{sgn}(\boldsymbol{g}^{(j+1/2)})$;
end
Output: Approximate scattering potential $\boldsymbol{f}^{(J_{\mathrm{IO}})}$.

For our specific application, the given data $\boldsymbol{d} = |\boldsymbol{D}(\boldsymbol{f})|$ corresponds to the measurement process modeled via $\boldsymbol{D}^{\mathrm{tot}}$ in (16). Since $\boldsymbol{D}^{\mathrm{tot}}$ is not invertible in general, we approximately compute $\boldsymbol{f}^{(j)}$ via Algorithm 2. The object domain constraints of $\boldsymbol{f}$ consist in the non-negativity and support constraint of the investigated physical object. Assuming that the support of f is constrained in the ball of radius r_{s}, we may enforce them by setting

$$\tilde{f}_{\boldsymbol{k}}^{(j)} := \begin{cases} \max\{f_{\boldsymbol{k}}^{(j)}, 0\}, & \|\boldsymbol{x}_{\boldsymbol{k}}\|_2 \leqslant r_{\mathrm{s}}, \\ 0, & \|\boldsymbol{x}_{\boldsymbol{k}}\|_2 > r_{\mathrm{s}}, \end{cases} \tag{28}$$

for $\boldsymbol{k} \in \mathcal{I}_K^d$. In the following, we refer to Algorithm 5 with the input rule $\boldsymbol{f}^{(j+1/2)} := \tilde{\boldsymbol{f}}^{(j)}$ as the *error-reduction algorithm (for ODT)*.

Instead of enforcing the object domain constrains strictly, the input of the next forward transform may be modified such that the output of the subsequent backward transform is pushed in direction of the feasible object signals. This procedure usually leads to a better numerical convergence of Algorithm 5. A typical choice of the next input $f^{(j+1/2)}$

is known as the *hybrid input-output* (HIO) by Fienup [28]. For some fixed $\beta \in (0, 1]$, the HIO step in Algorithm 5 consists of

$$f_{\boldsymbol{k}}^{(j+1/2)} := \begin{cases} f_{\boldsymbol{k}}^{(j)}, & \boldsymbol{k} \in \Gamma^{(j)}, \\ f_{\boldsymbol{k}}^{(j-1/2)} - \beta(f_{\boldsymbol{k}}^{(j)} - \tilde{f}_{\boldsymbol{k}}^{(j)}), & \boldsymbol{k} \in \mathcal{I}_K^d \backslash \Gamma^{(j)}, \end{cases} \tag{29}$$

where $\Gamma^{(j)} := \left\{\boldsymbol{k} \in \mathcal{I}_K^d : f_{\boldsymbol{k}}^{(j)} = \tilde{f}_{\boldsymbol{k}}^{(j)}\right\}$ consists of all indices $\boldsymbol{k}$ where $f_{\boldsymbol{k}}^{(j)}$ satisfies the object domain constraints. The next input $\boldsymbol{f}^{(j+1/2)}$ is thus composed of the input $\boldsymbol{f}^{(j-1/2)}$ and output $\boldsymbol{f}^{(j)}$ of the last forward-backward transform. We henceforth refer to Algorithm 5 with input rule (29) as the *HIO algorithm (for ODT)*.

The numerical performance of the error-reduction and the hybrid input-output algorithm may be increased by denoising the output of the forward-backward transform using the total variation. This idea has been successfully applied for example in Fourier and Fresnel diffraction imaging [30, 31]. If the inverse of the NDFT during the backward transform is computed by Algorithm 4, we automatically obtain a TV regularized output; so the backward transform corresponding to (23) goes hand in hand with the TV heuristic for the input-output phase retrieval methods.

7 Numerics of phase retrieval

In this section, we compare the performance of the CG method and the PD method in the context of phase retrieval in ODT, where we rely on the hybrid input-output algorithm in Section 6. In the second subsection, we compare our method with an existing one from literature, which only works well for a large distance r_{M} of the measurement plane.

7.1 Full diffraction model

We apply Algorithm 5 for the diffraction model $\boldsymbol{D}^{\mathrm{tot}}$. For the inversion of $\boldsymbol{D}^{\mathrm{tot}}$ required in each step of the input-output algorithm, we utilize either the CG method or the PD method with TV. We do not show the results with the BP method here, because it always performed worse than the CG. Since CG and PD are inside the loop of the input-output algorithm, the number of inner iterations can be reduced. In particular, the PD method in Algorithm 4 may be restarted in each step of the outer loop with the previous dual variable. Instead of restarting, the backtracking method may also be resumed, which significantly reduces the run time of the overall algorithm. Since the CG-based phase retrieval turns out to be much faster than the PD-based method, we utilize the CG phase reconstruction as starting point for phase retrieval with PD.

We employ the problem setting from Section 5.4. It is especially relevant for phase retrieval that the images are padded with zeros to represent the support constraints (28). We impose the support constraint $r_{\mathrm{s}} = 40$ in (28), which is larger than the

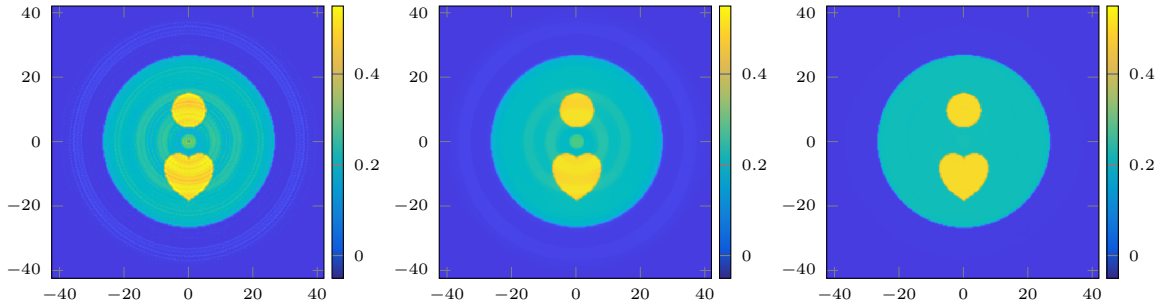

(a) HIO/CG reconstruction
$J_{\mathrm{IO}} = 10$, $J_{\mathrm{CG}} = 5$
PSNR 34.44, SSIM 0.821
0.6 sec

(b) HIO/CG and TVd
$\lambda = 0.05$, $J_{\mathrm{PD}} = 50$
PSNR 35.42, SSIM 0.831
0.1 sec

(c) HIO/PD with TV
λ=0.01, J_{IO}=20, J_{PD}=5
PSNR 41.32, SSIM 0.981
13 sec

Figure 8: HIO phase retrieval of $|\boldsymbol{D}^{\mathrm{tot}}\boldsymbol{f}|$ using CG in Alg. 3 and PD with TV in Alg. 4. The HIO/CG result is TV-denoised.

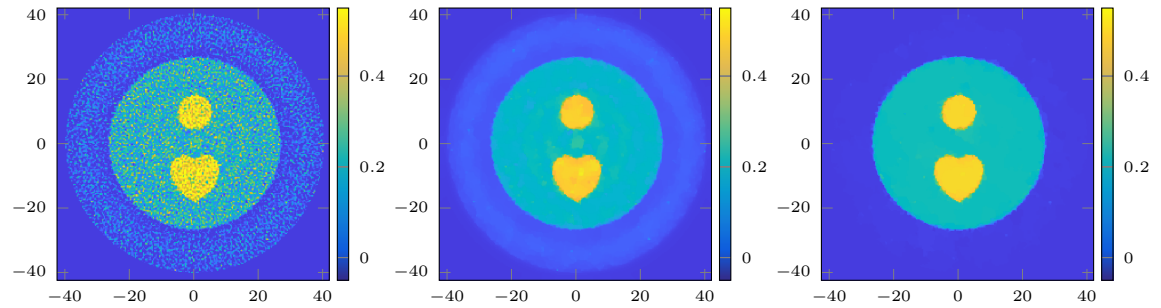

(a) HIO/CG reconstruction
$J_{\mathrm{IO}} = 10$, $J_{\mathrm{CG}} = 5$
PSNR 22.49, SSIM 0.354

(b) HIO/CG and TVd
$\lambda = 0.1$, $J_{\mathrm{PD}} = 50$
PSNR 28.38, SSIM 0.572

(c) HIO/PD with TV
$\lambda = 0.05$, J_{IO}=50, J_{PD}=10
PSNR 37.27, SSIM 0.936

Figure 9: HIO phase retrieval of $|\boldsymbol{D}^{\mathrm{tot}}\boldsymbol{f}|$ with 5% Gaussian noise using CG in Alg. 3 and PD with TV in Alg. 4. The HIO/CG result is TV-denoised.

actual support radius of the ground truth function of about 26. The results are shown in Figure 8, where the HIO is applied with the parameter $\beta = 0.7$. Especially for PD with TV, the result nearly coincides with the ground truth; so the missing phase does not decrease the image quality too much. With the CG method, there are some visible artifacts. However, executing more CG iterations may decrease the image quality because of the ill-posedness of the problem. The HIO/CG method coupled with TV denoising is outperformed by the HIO/PD method since the latter employs TV in each step of the outer iteration, while the former does it only once.

Adding 5 % additive Gaussian noise to the intensity data $|\boldsymbol{D}^{\mathrm{tot}}\boldsymbol{f}|$ does not decrease the reconstruction quality of HIO with TV-regularized PD inversion much, whereas the HIO reconstruction with CG becomes worse, see Figure 9. Raising the number of HIO iterations with CG results in even noisier reconstructions. For the PD method, the

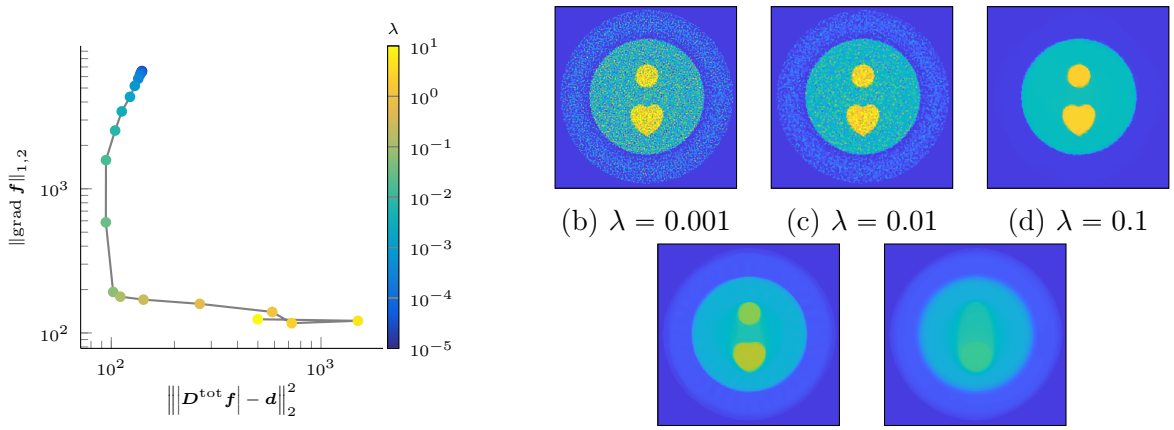

(a) L-curve

(b) $\lambda = 0.001$ (c) $\lambda = 0.01$ (d) $\lambda = 0.1$

(e) $\lambda = 1$ (f) $\lambda = 10$

Figure 10: L-curve for HIO/PD with TV in Figure 9c for $\lambda \in [10^{-5}, 10]$.

small number of inner iterations $J_{\text{PD}} = 10$ is sufficient because we restart the inner loop with the dual variables, parameters and initial solution from the previous outer step. Without this resuming, we need considerably more iterations, and even then the results are slightly worse, see Table 3.

	cold start with $J_{\text{PD}} =$				warm start
$J_{\text{IO}} = 50$	10	20	50	100	$J_{\text{PD}} = 10$
PSNR	29.64	35.10	36.34	36.44	37.12
SSIM	0.687	0.813	0.841	0.848	0.915

Table 3: Quality of the HIO/PD phase retrieval for cold start of the PD depending on the number of inner iterations J_{PD} and for the warm start (resuming with parameters, dual variable and initial solution of the previous step) as in Figure 9c.

The L-curve method does not formally apply to this setting since the regularization parameter λ appears only in the PD method and thus in the inner loop of Algorithm 5. However, we could still achieve some reasonable results, see Figure 10, where we plotted the residual $\||\boldsymbol{D}^{\text{tot}}\boldsymbol{f}| - \boldsymbol{d}\|_2^2$ versus the discrete TV semi-norm $\|\boldsymbol{f}\|_{2,1}$. Note that there is a different behavior of the residual for very small and very large λ, where the HIO algorithm fails to find the right phase. However, these values may be excluded since no meaningful reconstruction occurs.

For the three-dimensional simulations, we impose the support constraint $r_{\text{s}} = 40$ in (28). The reconstructions are shown in Figure 11. There are some artifacts in the HIO/CG reconstruction. Raising the number of HIO iterations in this case promotes further noise artifacts, since the data have been computed using a discretization of the convolution (4). The slight differences between the data and reconstruction model avoids the inverse crime. The HIO method with PD and TV overcomes this issue and produces excellent

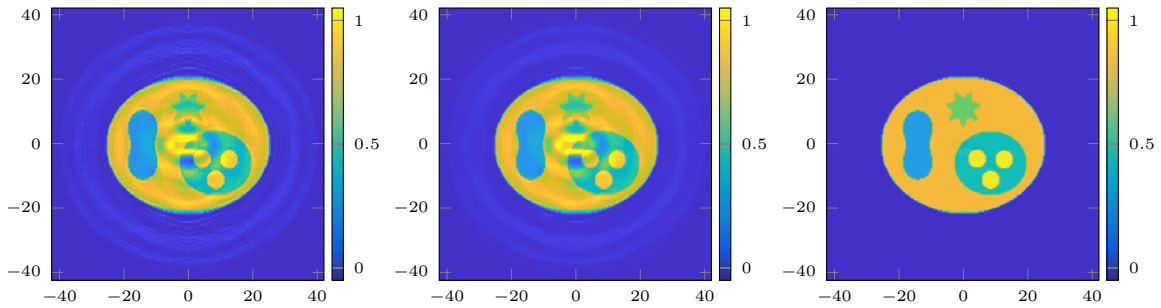

(a) HIO/CG reconstruction
$J_{\mathrm{IO}} = 10$, $J_{\mathrm{CG}} = 5$
PSNR 29.52, SSIM 0.713
5 min

(b) HIO/CG and TVd
$\lambda = 0.02$, $J_{\mathrm{TV}} = 20$
PSNR 29.88, SSIM 0.713
31 sec

(c) HIO/PD with TV
λ=0.01, J_{IO}=200, J_{PD}=5
PSNR 34.92, SSIM 0.994
3 h 48 min

Figure 11: Slice $x_3 = 0.35$ of the 3D HIO phase retrieval using CG in Alg. 3 and PD with TV in Alg. 4. The HIO/CG result is TV-denoised.

reconstructions comparable to the known-phase inversion. Adding more noise to the data has a similar effect to the reconstruction as in the two-dimensional case, see Figure 12.

7.2 Wave propagation–backpropagation method

In contrast to applying a phase retrieval method to the full ODT model $\boldsymbol{D}^{\mathrm{tot}}$, an alternative approach proposed by Maleki & Devaney [57] takes into account the physical nature of diffraction tomography. We call it the MD approach. It is also based on the input-output methods of Section 6, but instead of solving the whole ODT problem in each step, only the wave propagation in free space is considered. In particular, we define the free space wave propagation operator $\mathcal{P}$ for $v\colon \mathbb{R}^{d-1} \to \mathbb{C}$ by its Fourier transform

$$\mathcal{F}[\mathcal{P}v](\boldsymbol{y}') = \mathrm{e}^{\mathrm{i}\,\kappa(\boldsymbol{y}')\,r_{\mathrm{M}}}\,\mathcal{F}[v](\boldsymbol{y}'), \qquad \boldsymbol{y}' \in \mathbb{R}^{d-1},$$

where $\mathcal{F}$ denotes the $d-1$ dimensional Fourier transform. The inverse, the so-called free space backpropagation $\mathcal{P}^{-1}$, applied to the field $u_t^{\mathrm{sca}}(\cdot, r_{\mathrm{M}})$ is assumed to approximately match $u_t^{\mathrm{sca}}(\cdot, 0)$, which holds true for very thin samples. Then the support of

$$u_t^{\mathrm{sca}}(\cdot, 0) \approx \mathcal{P}^{-1}\big(u_t^{\mathrm{tot}}(\cdot, r_{\mathrm{M}}) - u^{\mathrm{inc}}(\cdot, r_{\mathrm{M}})\big)$$

is assumed to be contained in the ball of radius r_{s}.

Overall, the MD approach consists of two steps. First, we apply Algorithm 5 with $\boldsymbol{D}$ replaced by $\mathcal{P} + \mathrm{e}^{\mathrm{i}k_0 r_{\mathrm{M}}}$ to the data $|u_t^{\mathrm{tot}}(\cdot, r_{\mathrm{M}})|$ and impose that $u^{\mathrm{sca}}(\cdot, 0)$ has a compact support of radius r_{s}. In contrast to previous sections, we can assume neither the non-negativity nor the realness of $u^{\mathrm{sca}}(\cdot, 0)$. In the second step, we use an inversion method of Section 5 to recover f using the retrieved phase of u^{tot} from the first step.

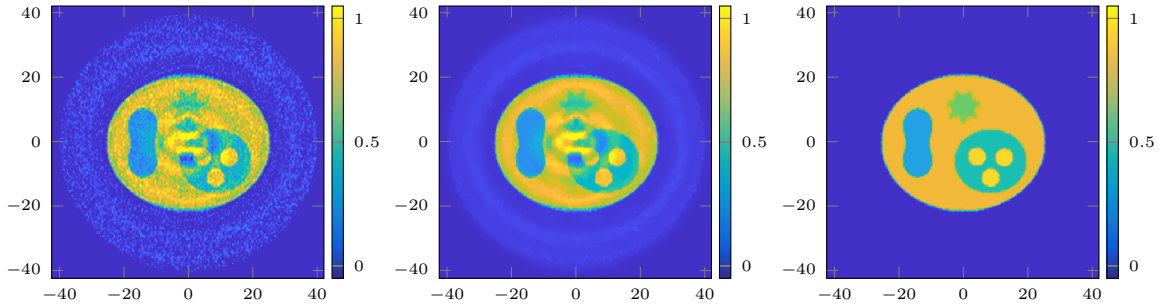

(a) HIO/CG reconstruction
$J_{\mathrm{IO}} = 10$, $J_{\mathrm{CG}} = 5$
PSNR 24.71, SSIM 0.589

(b) HIO/CG and TVd
$\lambda = 0.05$, $J_{\mathrm{PD}} = 20$
PSNR 27.16, SSIM 0.623

(c) HIO/PD with TV
λ=0.05, J_{IO}=200, J_{PD}=5
PSNR 34.10, SSIM 0.993

Figure 12: Slice $x_3 = 0.35$ of the 3D HIO phase retrieval with 5% Gaussian noise using CG in Alg. 3 and PD with TV in Alg. 4. The HIO/CG result is TV-denoised.

As pointed out in [57], this method works only well if the distance r_{M} of the measurement plane is very large, for instance $r_{\mathrm{M}} > 1000$. To obtain decent reconstructions, we require larger measurement plane sizes L_{M}. Consequently N has to becomes larger if the distance between neighboring grid points should stay the same as before.

For our numerical simulations, we chose $L_{\mathrm{M}} = 240$ and $r_{\mathrm{M}} = 1000$. Further, we raise the number of grid points to $N = 960$. The rest of the setting remains the same as in Section 7.1. The second step of the MD method is conducted with the inversion via PD with TV using $\lambda = 0.05$ and $J_{\mathrm{PD}} = 100$. The results are shown in Figure 13. We see that the MD approach requires a very high number of iterations to find a good solution. Even 20 000 iterations are not sufficient, but 50 000 yield a reasonable reconstruction.

For a smaller distance r_{M}, even more iterations are necessary. With $r_{\mathrm{M}} = 400$, we stopped after 5 million iterations, which took about 13 hours, and the reconstruction showed the right shape, but the level was still too low, see Figure 13d. In case of noisy data, we could not achieve a reasonable reconstruction with the MD approach.

8 Conclusion

We have compared reconstruction algorithms in ODT based on the Born approximation. For known-phase measurements, we compared the reconstruction based on three algorithms: the discrete backpropagation, the CG method, and the PD method with TV regularization. The backpropagation is the fastest, but the image quality was inferior compared to the others. The CG method was better and could still be improved when combined with TV denoising. In this case, the results are similar to the PD algorithm, which is usually the most accurate but also the slowest method.

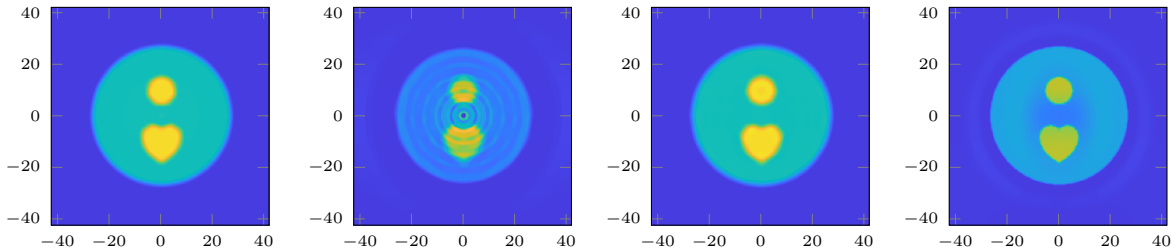

(a) HIO/PD with TV
$J_{\mathrm{IO}} = 50$, $J_{\mathrm{CG}} = 5$
PSNR 33.81
SSIM 0.945
34 sec

(b) MD retrieval
$J_{\mathrm{IO}} = 2 \cdot 10^4$
PSNR 21.74
SSIM 0.771
3 min 16 sec

(c) MD retrieval
$J_{\mathrm{IO}} = 5 \cdot 10^4$
PSNR 33.37
SSIM 0.937
8 min

(d) MD retrieval
$J_{\mathrm{IO}} = 5 \cdot 10^6$
PSNR 25.78
SSIM 0.867
13 h

Figure 13: MD phase retrieval with $r_{\mathrm{M}} = 1000$ (a)-(c) and $r_{\mathrm{M}} = 400$ (d).

For unknown phase, which causes the reconstruction problem to be more ill-posed, we achieved good results by applying the HIO algorithm, where the inner reconstruction is performed with the PD method. The image quality is comparable to the full phase inversion. The implementation with the CG method falls behind in terms of quality but, as it is much faster, gives good initial solutions for the HIO/PD method. By this procedure, the time requirements of PD are significantly reduced.

Acknowledgments

R. Beinert greatfully acknowledges funding by the BMBF under the project "VI-Screen" (13N15754). M. Quellmalz greatfully acknowledges funding by the DFG (STE 571/19-1, project number 495365311) within SFB F68 ("Tomography across the Scales").

References

[1] E. J. Akutowicz. "On the determination of the phase of a Fourier integral. I." *Trans. Amer. Math. Soc.* 83 (1956), pp. 179–192. DOI: 10.2307/1992910.

[2] B. Alexeev, A. S. Bandeira, M. Fickus, and D. G. Mixon. "Phase retrieval with polarization." *SIAM J. Imaging Sci.* 7.1 (2014), pp. 35–66. DOI: 10.1137/12089939X.

[3] A. H. Barnett, C. L. Epstein, L. F. Greengard, and J. F. Magland. "Geometry of the phase retrieval problem." *Inverse Problems* 36.9 (2020), pp. 094003, 37. DOI: 10.1088/1361-6420/aba5ed.

[4] H. H. Bauschke and P. L. Combettes. *Convex Analysis and Monotone Operator Theory in Hilbert Spaces*. CMS Books in Mathematics/Ouvrages de Mathématiques de la SMC. New York: Springer, 2011, pp. xvi+468. DOI: 10.1007/978-1-4419-9467-7.

[5] R. Beinert and K. Bredies. "Tensor-free proximal methods for lifted bilinear/quadratic inverse problems with applications to phase retrieval." *Found. Comput. Math.* 21.5 (2021), pp. 1181–1232. DOI: 10.1007/s10208-020-09479-4.

[6] R. Beinert and G. Plonka. "Ambiguities in one-dimensional discrete phase retrieval from Fourier magnitudes." *J. Fourier Anal. Appl.* 21.6 (2015), pp. 1169–1198. DOI: 10.1007/s00041-015-9405-2.

[7] R. Beinert and G. Plonka. "One-dimensional discrete-time phase retrieval." In: *Nanoscale Photonic Imaging*. Topics in Applied Physics 134. Springer, Cham, 2020, pp. 603–627. DOI: 10.1007/978-3-030-34413-9_24.

[8] T. Bendory, R. Beinert, and Y. C. Eldar. "Fourier phase retrieval: uniqueness and algorithms." In: *Compressed sensing and its applications*. Appl. Numer. Harmon. Anal. Birkhäuser/Springer, Cham, 2017, pp. 55–91.

[9] G. Beylkin. "On the fast Fourier transform of functions with singularities." *Appl. Comput. Harmon. Anal.* 2 (1995), pp. 363–381. DOI: 10.1006/acha.1995.1026.

[10] K. Bredies and M. Holler. "Higher-order total variation approaches and generalisations." *Inverse Problems* 36.12 (2020), pp. 123001, 128. ISSN: 0266-5611. DOI: 10.1088/1361-6420/ab8f80.

[11] K. Bredies and D. Lorenz. *Mathematical Image Processing*. Applied and Numerical Harmonic Analysis. Cham: Birkhäuser/Springer, 2018. DOI: 10.1007/978-3-030-01458-2.

[12] E. Candès, L. Demanet, and L. Ying. "A fast butterfly algorithm for the computation of Fourier integral operators." *Multiscale Model. Simul.* 7.4 (2009), pp. 1727–1750. ISSN: 1540-3459. DOI: 10.1137/080734339.

[13] E. J. Candès, Y. C. Eldar, T. Strohmer, and V. Voroninski. "Phase retrieval via matrix completion." *SIAM J. Imaging Sci.* 6.1 (2013), pp. 199–225. DOI: 10.1137/110848074.

[14] E. J. Candès, T. Strohmer, and V. Voroninski. "PhaseLift: exact and stable signal recovery from magnitude measurements via convex programming." *Comm. Pure Appl. Math.* 66.8 (2013), pp. 1241–1274. DOI: 10.1002/cpa.21432.

[15] A. Chambolle, V. Caselles, D. Cremers, M. Novaga, and T. Pock. "An introduction to total variation for image analysis." In: *Theoretical Foundations and Numerical Methods for Sparse Recovery*. Ed. by M. Fornasier. De Gruyter, 2010, pp. 263–340. DOI: 10.1515/9783110226157.263.

[16] J. Cheng and S. Han. "Diffraction tomography reconstruction algorithms for quantitative imaging of phase objects." *J. Opt. Soc. Am. A* 18.7 (2001), pp. 1460–1464. DOI: 10.1364/JOSAA.18.001460.

[17] G. Chierchia, E. Chouzenoux, P. L. Combettes, and J.-C. Pesquet. "The Proximity Operator Repository. User's guide." proximity-operator.net.

[18] D. Colton and R. Kress. *Inverse Acoustic and Electromagnetic Scattering Theory*. 3rd ed. Applied Mathematical Sciences 93. Berlin: Springer, 2013. ISBN: 978-1-4614-4941-6. DOI: 10.1007/978-1-4614-4942-3.

[19] A. Devaney. "A filtered backpropagation algorithm for diffraction tomography." *Ultrason. Imaging* 4.4 (1982), pp. 336–350. DOI: 10.1016/0161-7346(82)90017-7.

[20] A. Dutt and V. Rokhlin. "Fast Fourier transforms for nonequispaced data." *SIAM J. Sci. Stat. Comput.* 14 (1993), pp. 1368–1393. DOI: 10.1137/0914081.

[21] D. Edidin. "The geometry of ambiguity in one-dimensional phase retrieval." *SIAM J. Appl. Algebra Geom.* 3.4 (2019), pp. 644–660. DOI: 10.1137/18M1230530.

[22] P. Elbau, M. Ritsch-Marte, O. Scherzer, and D. Schmutz. "Motion reconstruction for optical tomography of trapped objects." *Inverse Problems* 36.4 (2020), p. 044004. ISSN: 0266-5611. DOI: 10.1088/1361-6420/ab67db.

[23] H. W. Engl, M. Hanke, and A. Neubauer. *Regularization of Inverse Problems*. Vol. 375. Mathematics and Its Applications. Kluwer Academic Publishers, 1996. ISBN: 0-7923-4157-0.

[24] S. Fan, S. Smith-Dryden, G. Li, and B. E. A. Saleh. "An iterative reconstruction algorithm for optical diffraction tomography." In: *IEEE Photonics Conference (IPC)*. 2017, pp. 671–672. DOI: 10.1109/ipcon.2017.8116276.

[25] A. Fannjiang and W. Liao. "Fourier phasing with phase-uncertain mask." *Inverse Problems* 29.12 (2013), pp. 125001, 21. DOI: 10.1088/0266-5611/29/12/125001.

[26] A. Fannjiang and T. Strohmer. "The numerics of phase retrieval." *Acta Numer.* 29 (2020), pp. 125–228. DOI: 10.1017/s0962492920000069.

[27] F. Faucher, C. Kirisits, M. Quellmalz, O. Scherzer, and E. Setterqvist. "Diffraction tomography, Fourier reconstruction, and full waveform inversion." *ArXiv e-prints* (2021). arXiv: 2110.07921.

[28] J. R. Fienup. "Phase retrieval algorithms: a comparison." *Appl. Opt.* 21.15 (1982), pp. 2758–2769. DOI: 10.1364/AO.21.002758.

[29] J. R. Fienup. "Reconstruction of an object from the modulus of its fourier transform." *Opt. Lett.* 3.1 (1978), pp. 27–29. DOI: 10.1364/OL.3.000027.

[30] C. Gaur and K. Khare. "Sparsity-assisted phase retrieval in the Fresnel zone." *J. Modern Opt.* 66.12 (2019), pp. 1296–1304. DOI: 10.1080/09500340.2019.1615142.

[31] C. Gaur, B. Mohan, and K. Khare. "Sparsity-assisted solution to the twin image problem in phase retrieval." *J. Opt. Soc. Am. A* 32.11 (2015), pp. 1922–1927. DOI: 10.1364/JOSAA.32.001922.

[32] G. Gbur and E. Wolf. "Hybrid diffraction tomography without phase information." *J. Opt. Soc. Am. A* 19.11 (2002), pp. 2194–2202. DOI: 10.1364/OL.27.001890.

[33] R. W. Gerchberg and W. O. Saxton. "A practical algorithm for the determination of phase from image and diffraction plane pictures." *Optik* 35.2 (1972), pp. 237–246.

[34] T. Goldstein, M. Li, and X. Yuan. "Adaptive primal-dual splitting methods for statistical learning and image processing." In: *Advances in Neural Information Processing Systems*. Ed. by C. Cortes, N. Lawrence, D. Lee, M. Sugiyama, and R. Garnett. Vol. 28. 2015, pp. 2089–2097.

[35] I. S. Gradshteyn and I. M. Ryzhik. *Table of Integrals, Series, and Products*. Seventh. Academic Press New York, 2007.

[36] P. Grohs, S. Koppensteiner, and M. Rathmair. "Phase retrieval: uniqueness and stability." *SIAM Rev.* 62.2 (2020), pp. 301–350. DOI: 10.1137/19M1256865.

[37] T. E. Gureyev, T. J. Davis, A. Pogany, S. C. Mayo, and S. W. Wilkins. "Optical phase retrieval by use of first Born- and Rytov-type approximations." *Appl. Opt.* 43.12 (2004), pp. 2418–2430. DOI: 10.1364/AO.43.002418.

[38] M. Hanke. *Conjugate Gradient Type Method for Ill-posed Problems*. New York, NY, USA: Wiley, 1995.

[39] P. C. Hansen. "Analysis of discrete ill-posed problems by means of the L-curve." *SIAM Rev.* 34.4 (1992), pp. 561–580. ISSN: 0036-1445, 1095-7200. DOI: 10.1137/1034115.

[40] R. Hielscher and M. Quellmalz. "Optimal mollifiers for spherical deconvolution." *Inverse Problems* 31.8 (2015), p. 085001. DOI: 10.1088/0266-5611/31/8/085001.

[41] L. Hörmander. *The Analysis of Linear Partial Differential Operators: Distribution Theory and Fourier Analysis*. Springer-Verlag, 1990. DOI: 10.1007/978-3-642-61497-2.

[42] R. Horstmeyer, J. Chung, X. Ou, G. Zheng, and C. Yang. "Diffraction tomography with Fourier ptychography." *Optica* 3.8 (2016), pp. 827–835. DOI: 10.1364/OPTICA.3.000827.

[43] K. Jalalzai. "Some remarks on the staircasing phenomenon in total variation-based image denoising." *J. Math. Imaging Vision* 54.2 (2016), pp. 256–268.

[44] P. Jaming. "Uniqueness results in an extension of Pauli's phase retrieval problem." *Appl. Comput. Harmon. Anal.* 37.3 (2014), pp. 413–441. DOI: 10.1016/j.acha.2014.01.003.

[45] A. C. Kak and M. Slaney. *Principles of Computerized Tomographic Imaging*. New York, NY, USA: IEEE Press, 1987. DOI: 10.1137/1.9780898719277.

[46] J. Keiner, S. Kunis, and D. Potts. *NFFT 3.5, C subroutine library*. http://www.tu-chemnitz.de/~potts/nfft. Contributors: F. Bartel, M. Fenn, T. Görner, M. Kircheis, T. Knopp, M. Quellmalz, M. Schmischke, T. Volkmer, A. Vollrath.

[47] J. Keiner, S. Kunis, and D. Potts. "Using NFFT3 - a software library for various nonequispaced fast Fourier transforms." *ACM Trans. Math. Software* 36 (2009), Article 19, 1–30. DOI: 10.1145/1555386.1555388.

[48] C. Kirisits, M. Quellmalz, M. Ritsch-Marte, O. Scherzer, E. Setterqvist, and G. Steidl. "Fourier reconstruction for diffraction tomography of an object rotated into arbitrary orientations." *Inverse Problems* 37.11 (2021), p. 115002. ISSN: 0266-5611. DOI: 10.1088/1361-6420/ac2749.

[49] M. V. Klibanov and V. G. Kamburg. "Uniqueness of a one-dimensional phase retrieval problem." *Inverse Problems* 30.7 (2014), pp. 075004, 10. DOI: 10.1088/0266-5611/30/7/075004.

[50] M. V. Klibanov, P. E. Sacks, and A. V. Tikhonravov. "The phase retrieval problem." *Inverse Problems* 11.1 (1995), pp. 1–28.

[51] T. Knopp, S. Kunis, and D. Potts. "A note on the iterative MRI reconstruction from nonuniform k-space data." *Int. J. Biomed. Imag.* 2007 (2007). ID 24727. DOI: 10.1155/2007/24727.

[52] S. G. Krantz and H. R. Parks. *A Primer of Real Analytic Functions*. 2nd. Birkhäuser Advanced Texts. Boston: Birkhäuser, 2002. DOI: 10.1007/978-0-8176-8134-0.

[53] M. Kujawińska, W. Krauze, A. Kus, J. Kostencka, T. Kozacki, B. Kemper, and M. Dudek. "Problems and solutions in 3-d analysis of phase biological objects by optical diffraction tomography." *Int. J. Optomechatronics* 8 (2014), pp. 357–372. DOI: 10.1080/15599612.2014.942934.

[54] S. Kunis and D. Potts. "Stability results for scattered data interpolation by trigonometric polynomials." *SIAM J. Sci. Comput.* 29 (2007), pp. 1403–1419. DOI: 10.1137/060665075.

[55] Y. Li, H. Yang, and L. Ying. "A multiscale butterfly algorithm for multidimensional Fourier integral operators." *Multiscale Model. Simul.* 13.2 (2015), pp. 614–631. ISSN: 1540-3459. DOI: 10.1137/140997658.

[56] P. Y. Liu et al. "Cell refractive index for cell biology and disease diagnosis: past, present and future." *Lab Chip* 16.4 (2016), pp. 634–644. DOI: 10.1039/C5LC01445J.

[57] M. H. Maleki and A. J. Devaney. "Phase-retrieval and intensity-only reconstruction algorithms for optical diffraction tomography." *J. Opt. Soc. Am. A* 10.5 (1993), p. 1086. DOI: 10.1364/josaa.10.001086.

[58] S. Maretzke. "Locality estimates for Fresnel-wave-propagation and stability of x-ray phase contrast imaging with finite detectors." *Inverse Problems* 34.12 (2018), p. 124004. DOI: 10.1088/1361-6420/aae78f.

[59] P. Müller, M. Schürmann, and J. Guck. "ODTbrain: a Python library for full-view, dense diffraction tomography." *BMC Bioinform.* 16 (367 2015). DOI: 10.1186/s12859-015-0764-0.

[60] F. Natterer and F. Wübbeling. *Mathematical Methods in Image Reconstruction*. Philadelphia, PA: SIAM, 2000. DOI: 10.1137/1.9780898718324.fm.

[61] G. E. Pfander and P. Salanevich. "Robust phase retrieval algorithm for time-frequency structured measurements." *SIAM J. Imaging Sci.* 12.2 (2019), pp. 736–761. DOI: 10.1137/18M1205522.

[62] G. Plonka, D. Potts, G. Steidl, and M. Tasche. *Numerical Fourier Analysis*. Applied and Numerical Harmonic Analysis. Birkhäuser, 2018. ISBN: 978-3-030-04305-6. DOI: 10.1007/978-3-030-04306-3.

[63] D. Potts and G. Steidl. "A new linogram algorithm for computerized tomography." *IMA J. Numer. Anal.* 21 (2001), pp. 769–782.

[64] G. Steidl. "A note on fast Fourier transforms for nonequispaced grids." *Adv. Comput. Math.* 9 (1998), pp. 337–353. DOI: 10.1023/A:1018901926283.

[65] A. Walther. "The question of phase retrieval in optics." *Optica Acta* 10 (1963), pp. 41–49. DOI: 10.1080/713817747.

[66] Z. Wang, A. C. Bovik, H. R. Sheikh, and E. P. Simoncelli. "Image quality assessment: from error visibility to structural similarity." *IEEE Trans. Image Process.* 13 (2004), pp. 600–612. DOI: 10.1109/TIP.2003.819861.

[67] T. C. Wedberg and J. J. Stamnes. "Comparison of phase retrieval methods for optical diffraction tomography." *Pure Appl. Opt.* 4 (1995), pp. 39–54. DOI: 10.1088/0963-9659/4/1/005.

[68] T. Yokota and H. Hontani. "An efficient method for adapting step-size parameters of primal-dual hybrid gradient method in application to total variation regularization." In: *2017 Asia-Pac. Signal Inf. Process. Assoc. Annu. Summit Conf. (APSIPA ASC)*. 2017, pp. 973–979. DOI: 10.1109/APSIPA.2017.8282164.